ORIGINAL ARTICLE

Tribomechanical analysis and machining development for TiSiCN material deposited on industrial steel

Erick Hernandez-Renjifo[1] · Christian Ortíz[1] · Julio Cesar Caicedo[1] · Luis Alfredo Rodríguez[2,3] · Cesar Magén[4,5]

Abstract

In recent years, nanocomposite coatings have become relevant in different metal-mechanical processes related to the increase of the tribomechanical properties. Therefore, this research is focused on improving mechanical behavior and wear resistance of TiSiCN nanocomposite coating with different power applied on the silicon nitride (Si_3N_4) target by means of magnetron sputtering r.f. technique and synthesized on HSS (high-speed steel) and oriented silicon (100) substrates. The response of the nanocomposite coatings to power variation was analyzed by X-ray diffraction (XRD), X-ray photoelectron spectroscopy (XPS), scanning electron microscopy (SEM), transmission electron microscopy (TEM), atomic force microscopy (AFM), and instrumented nanoindentation. Ball-on-disc and scratch tests were used for tribological characterization. The XRD study determined an FCC structure with a peak of maximum intensity in the plane (200). XPS analysis showed chemical energies in the bonds and stoichiometry. By means of the AFM technique, the tendency to decrease the roughness and grain size was detected, with the increase of the power for the coatings obtained at 500 W. From the nanoindentation test, it was possible to stablish increases in mechanical properties as the applied power increases; the best performance was obtained for coating with a 500-W power, where the hardness and elastic modulus were 32 GPa and 301 GPa, respectively. The friction coefficient in dry environment decreased with increasing applied power (500 W, 0.31), and the critical load produced by adhesive wear was determined for the TiSiCN nanocomposite coatings for the different applied powers, showing the highest critical load in the coating with 500 W (62.42 N). Finally, the cutting tests with AISI 1020 steel (workpiece) to assess wear as a function of the applied power. A comparison of the tribological properties revealed a decrease of flank wear (approximately 37%) for ASSAB 17 steel burins coated with TiSiCN nanocomposite coatings with 550 W, when compared to uncoated ASSAB 17 steel burins. These results open a great industrial potential in anti-wear applications.

Keywords Nanocomposites · Physical vapor deposition · TiSiCN · Tribological properties · Machining tools

✉ Julio Cesar Caicedo
jcaicedoangulo1@gmail.com

1 Tribology, Powder Metallurgy and Processing of Solid Recycled Research Group, Universidad del Valle, Cali, Colombia

2 Departamento de Física, Universidad del Valle, A.A, 25360 Cali, Colombia

3 Centro de Excelencia en Nuevos Materiales, Universidad del Valle, A.A, 25360 Cali, Colombia

4 Instituto de Nanociencia y Materiales de Aragón (INMA)–Departamento de Física de la Materia Condensada, Universidad de Zaragoza, 50009 Zaragoza, Spain

5 Laboratorio de Microscopía Avanzadas (LMA), Universidad de Zaragoza, 50018 Zaragoza, Spain

1 Introduction

The metal-mechanical sector is one of the strategic sectors worldwide; in most countries, some companies base their production in the metal transformation sector, specifically in machining, cutting, forming, and stamping processes that demand a high consumption of tooling for their production [1]. Due to this need, the industrial sector has been promoting the development of new technologies in processes and materials that allow a continuous improvement of the processes. An alternative lies in the development of coatings that extend the life of the components used in the different production processes [2–4]. The development of hard coatings comes from the year 1980 approximately, with the obtaining of commercial coatings such as titanium nitride (TiN) and titanium carbide (TiC) that were synthesized

through physical vapor deposition (PVD) technique and then followed by increasingly advanced coatings in their mechanical, chemical, physical, tribological, and electrochemical properties until reaching novel properties which have been found in multilayer coatings (multilayer type) and nanocomposites, which could reach hardness similar to diamond (100 GPa) [1]. Among the most striking properties of nanostructured materials (nanocomposites) is the considerable increase in hardness, which becomes more evident in thin layers composed of nanocrystals of carbides or nitrides immersed in a nanocrystalline or amorphous matrix [5–7]. Taking into account the above, nanocomposite coatings achieve excellent tribomechanical performance due to the restriction of the origin and displacement of dislocations; this movement is blocked by refined grains and spacing between them, originating incoherent deformations. As the grain size decreases, the activity of interfaces is increased, reducing the ductility of the coating and minimizing the stacking failure energy. Additionally, these coatings are characterized by increasing the number of restrictions with a crystalline/amorphous transition across the grain boundary, limiting the formation and crack propagation [7, 8]. Quaternary single-layer coatings based on carbonitrides and transition metals, such as titanium silicon carbonitride (TiSiCN), do not have detailed studies of their mechanical and tribological properties. Currently, some studies on TiSiCN coatings have been reported by techniques such as reactive arc and cathodic arc with some progress in their characterization [5, 9–11]. In the literature, there are reports of the synthesis of TiSiCN material evidencing diverse physical and mechanical properties, where, for example in the work of Marchin and Ashrafizadeh [12], the effect of carbon addition on tribological performance of TiSiN coatings produced by cathodic is reported; the work of Johnson et al. [13] presents a study of the microstructure evolution and age hardening in (Ti,Si)(C,N) thin films deposited by cathodic arc evaporation; on the other hand, Lin et al. [14] reported advances in the development and evaluation of low friction TiSiCN nanocomposite coatings for piston ring applications; finally, Thangavel et al. [15] demonstrate in detail the synthesis and characterization of Ti-Si-C-N nanocomposite coatings prepared by a filtered vacuum arc method. In this sense, in all the reported works, it can be evidenced the relationship between the physical properties and the relationship between the microstructure of the nanocomposites and the chemical composition. Therefore, all studies have allowed extending the knowledge of the quaternary TiSiCN coating with analysis about some mechanical properties. Taking into account the last discussion in the present research, the main goal is to present a deep nanostructural characterization about the mechanical-tribological behavior with an analysis of the wear rate of the [nc-TiSiCN]-[a-SiCN] nanocomposite coating deposited on industrial steel with the variation of

the applied power on the Si_3N_4 target; thus, the tribological properties revealed a decrease of flank wear for ASSAB 17 steel burins coated with TiSiCN nanocomposite coatings, when compared to uncoated ASSAB 17 steel burins. These results open a great industrial potential in anti-wear applications, providing an industrial alternative in metal-mechanical components that require a high performance related to the increase hardness, elastic modulus, and wear resistance, among others.

2 Experimental details

2.1 Coating deposition

The coatings were prepared from PVD technique with r.f source, and different substrates were used such as silicon (100) wafer and steel HSS. The targets used in this study were TiC and Si_3N_4 with a purity of 99.9% for both and with diameters of 10 cm each target located frontally inside the PVD chamber, purchased from Kurt J. Lesker Company. The silicon substrates were purchased from NanoInk Company, and Ar^+ gas was obtained from AGA FANO S.A. Company. The substrates were ultrasonically cleaned in isopropanol and acetone for 15 min each. To guarantee optimum working conditions and ensure a low level of contamination, a background pressure of 2.0×10^{-6} mbar was obtained, thus ensuring a high vacuum. The metallic substrate used in this study had a disc-type geometry with a diameter of 1 cm. The sputtering gas was Ar^+ with 50 sccm with a total working pressure of 5×10^{-3} mbar. An unbalanced r.f. bias voltage was applied, which generated a negative signal fixed at −20 V. During the deposition, a power of 400 W was used for the TiC target, and for the Si_3N_4 target, the power was varied from 400, 450, 500 up to 550 W. In this sense, in the current work, the power densities were adjusted with values of 5.1 W/cm^2, 5.7 W/cm^2, 6.4 W/cm^2, and 7.0 W/cm^2 for the growth of the TiSiCN layer; the distance between substrate and target was 6 cm. Additionally, inside the chamber, a temperature of 250 °C was preserved. Therefore, the synthesis of the TiSiCN materials was carried out by rotating the substrates within the co-sputtering process from the plasma generated from the simultaneous sputtering of the TiC target and the SiCN target. Finally, the substrate spinning system maintained a speed of 60 rpm for each deposited coating, obtaining thicknesses close to 2.0 μm.

2.2 Characterization techniques

The microstructures of the coatings were investigated using a PANalytical X'Pert Pro X-ray diffractometer equipment with Cu-Kα radiation ($\lambda = 1.5406$ Å) in the Bragg-Brentano (θ/2θ) scan mode with high angle segment. The thicknesses

of the coatings, tribological surfaces, and the flank wear (VB) were measured using the scanning electron microscopy (SEM) (JSM 6490LV JEOL), with a magnification interval between ×525 and ×24,000. The thicknesses of the coatings were corroborated by profilometry, and the chemical characterization and the bonding structure were analyzed by X-ray photoelectron spectroscopy (XPS, SAGE HR 100 (SPECSTM)). The excitation source is monochromatic Al Kα radiation ($h\upsilon$ = 1486.6 eV), and the anode power is 150 W. All spectra are collected at normal emission angle. The base pressure during spectra acquisition is lower than 1.1×10^{-9} Torr (1.5×10^{-7} Pa). The analyzer pass energy is set to 20 eV, which results in that the spectrometer energy resolution determined from the FE cut-off of Ti and Si samples is 0.38 eV.

The calibration of the binding energy (BE) scale was confirmed by examining sputter-cleaned method for Ti-Si-C-N samples (all in the form of polycrystalline thin films). So the BE scale referencing based on the C 1s peak of AdC is part of both ASTM and ISO standards [16–19]; moreover, the calibration of the binding energy scale was confirmed by examining sputter-cleaned Au, Ag, and Cu samples according to the recommended ISO standards for monochromatic Al Kα sources that place Au 4f7/2, Ag 3d5/2, and Cu 2p3/2 peaks at 83.96, 368.21, and 932.62 eV, respectively [20, 21]. In this sense, this method for calibrating instrumental binding energy scales uses metallic samples of pure copper (Cu), silver (Ag), and gold (Au) and is applicable to X-ray photoelectron spectrometers with unmonochromated aluminum (Al) or magnesium (Mg) X-rays or monochromated Al X-rays. It is valid for the binding energy range of 0 to 1040 eV [21, 22]. Therefore, the binding energy scale for Ti, Si, and N was confirmed by examining sputter-cleaned method. For all measurements on sapphire, the charge neutralizer is used. Work function ϕ_{SA} measurements by ultraviolet photoelectron spectroscopy (UPS) are performed in the same instrument [16, 23, 24]. A local exploration of the microstructure was carried out through high-resolution transmission electron microscopy (HR-TEM, FEI Titan3 60-300), an aberration-corrected TEM operated at 300 kV. For performing TEM experiments, a cross-sectional lamella was prepared by using a Helios Nanolab 600 dual beam system. Grain size and roughness were measured on AFM (Asylum Research MFP-3D®) micrographs by image processor (SPIP®) software. The hardness and elastic modulus and the load discharge curves were determined by a nanoindentation instrument (Ubil-Hystron model) with a variable load Berkovich diamond indenter. To evaluate the tribological behavior of TiSiCN coatings following ASTM G99-17 [14], the ball-on-disc (MT 4001-98 model) wear was used against hardened steel ball (100Cr6), with a load of 5 N, sliding distance of 500 m, and angular speed of 160 rpm, without lubrication. Finally, the load capacity was performed

according to ASTM G171-03 [25, 26]; using a scratching equipment (Microtest MTR2 model), the scratching length was 6 mm with a maximum load of 90 N and step of 1.97 mm/min, to determine the critical load for coating failure.

2.3 Materials and methods for TiSiCN coating wear tests

Wear tests of ASSAB 17 steel burins coated with TiSiCN nanocomposite coatings were carried out by using AISI 1020 steel as work material to be machined. This AISI 1020 steel is used broadly in high-mechanical performance pieces, especially in the automotive industry. For experimental development, this work used a high-speed cutting (HSC) regime in the cylindrical turning for this coated ASSAB 17 steel machining tool for the burin processes. This technology was applied to diminish machining times and improve surface finish, as well as to permit the elaboration of hardened pieces, even facilitating the development of devices in a single run in the machine.

The values for the parameters used are shown in Table 1. In this work, it was selected the high-speed cutting (HSC) regime defined as machining at high cutting speeds (spindle speeds) and/or at high feed rates in order to achieve short machining, or lead times, taking into account the type of material to be machined (soft or hard machining), cutting materials, and metal removal rate.

The cutting tool materials were ASSAB 17 steel burins, because they are high alloyed cobalt high steel speed with excellent cutting properties, wear resistance, toughness, and heat resistance. The cutting tool geometry for the ASSAB 17 burin consists of a sharpened cutting part called its point and the shank, associated to the lateral cutting area tool geometry which is made up of shank, base, face, flank, heel, nose, back rake angle, side rake angle, side clearance, wide cutting edge, end cutting edge, and lip angle. To remove a metal chip from a workpiece, the tools have to cut along at least 2 surfaces: a main cutting edge and an auxiliary cutting edge. The main cutting edge cuts the main portion of the chip while the auxiliary cuts the second surface and removes the material. The tool tip is bounded by the face (along which the chip slides as they are cut by the tool), the side flank or major flank the end flank or minor flank and the base. The cutting tools ASSAB 17 steels were commercially obtained from Sandvik Coromant® catalogue.

Table 1 Values assigned for the parameters in the machining process associated to straight turning for rough cut

Parameter	Description
Cutting speed (Vc)	110 m/min
Feed rate (d)	0.5 mm/rev.
Depth of cut (doc)	0.5 mm
Coolant	Dry

In dry machining processes of carbon steels, it is convenient to use HSS cutting tools (ASSAB 17) coated with hard coatings, e.g. nanocomposite materials because they are more economical procedures in relation to WC insert. This economical reduction is associated to the tool value and the process efficiency which are increased due to the high surface hardness conferred by the coating generating low friction coefficients, low work temperatures with heat dissipation transferred to the chip, and low wear rates on the tool with better surface finish on the workpiece.

The workpieces were AISI 1020 steels, taking into account that it is a low carbon steel, easy to machine, and with good weldability. Due to its carbon content, these steels are used for the manufacture of structural parts or medium-strength machinery with a Brinell 260 (HB) or Vickers hardness of 273.75 (HV10). The geometry of the workpiece was cylindrical bars with diameters of 25.4 mm and a length of 2 m.

In order to obtain the cutting length and flank wear (VB), it was necessary to take into account Eq. (1):

$$N = \frac{1000 \cdot V_c}{\pi \cdot D} \quad (1)$$

where N is the rotational speed (in rpm), Vc is the cutting speed (in m/min), and D is the diameter of the machining to be performed (in mm). Therefore, from the cutting speed (Vc), the cutting length was determined such as is present in Table 1. So this machining methodology permits the comparison of wear behavior results under similar working conditions. Finally, for wear measurements of coated ASSAB 17 steel, a SEM was employed to analyze the flank wear.

3 Results and discussion

3.1 X-ray diffraction (XRD)

Figure 1a shows X-ray diffraction patterns of TiSiCN coatings obtained at different power values applied to the Si_3N_4 target, which were deposited on silicon substrates with (100) orientation. This quaternary coating was indexed with two different files attributed to TiC and Si_3N_4 compounds, respectively, which correspond to the stoichiometries of the targets. These diffraction peaks are characteristic to the presence of distinct compounds; the Bragg peaks located in the (111), (200), (220), (311), and (222) planes for the angles 36.04°, 41.98°, 60.89°, 72.67°, and 76.08° are attributed to the TiC compound, which presents an FCC structure with an Fm3m space group according to the JCPDF 00-001-2122 index file. The peaks (111), (200), and (220) are also characteristic of Ti(C, N) phases as reported by Marchin and Ashrafizadeh [12]. Moreover, the presence of the Si_3N_4 compound as evidenced by the reflections in the characteristic planes (101), (301), and (321) for the angles 33.56°, 52.13°, and 70.11°, respectively, presents a hexagonal structure with a P63/m space group corresponding to the JCPDF 00-009-0259 index file, a phase related to this structure as evidenced by several researchers [13–15, 27]. However, it is important to highlight that some authors have reported some nanocrystalline phases associated with the TiSiCN composite, which presents a direction (200) of a cubic TiSiCN embryonic phase coming from the FCC structure of TiC [12]. Moreover, the TiSiCN cubic crystal presents a lattice parameter of 4.2791 Å and the interplanar distance of $d_{(200)} = 2.1395$ Å, which is different from
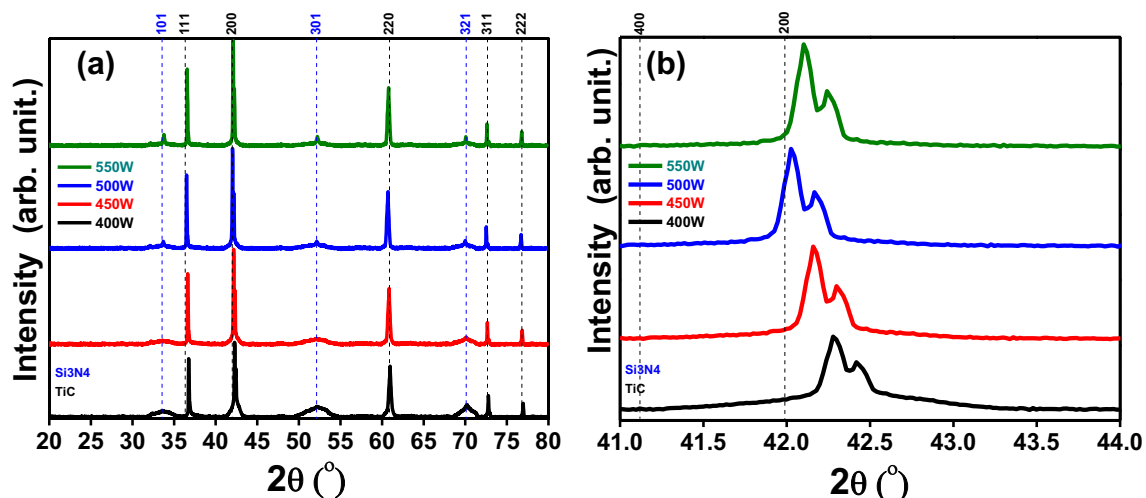

Fig. 1 X-ray diffraction patterns for TiSiCN coatings: **a** diffraction patterns as a function of applied power on the Si_3N_4 target and **b** intensity maxima of all layers, for the (200) plane inscribed in a compressive stress region

the lattice parameter and the interplanar distance values for the TiC material ($a_0 = 4.6000$ Å, $d_{(200)} = 2.3300$ Å). Figure 1b shows the magnification of the maximum intensity peak corresponding to the 200 plane for all coatings. In addition, the position of the structure is stress-free (dotted line) according to the international files. These results showed that the TiSiCN coating deposited with an applied power of 400 W presents a shift to the right in relation to the stress-free position; this peak shift is associated to the presence of compressive residual stresses within the crystalline structure during the deposition process, which cause a distortion of the crystalline structure. Subsequently, with the increase of the applied power to the Si_3N_4 target at 500 W, a displacement or approach of the peaks of maximum intensity towards values where the material is stress-free (dotted line) was evidenced. This behavior is attributed to a relaxation of the compressive residual stresses within the crystalline structure. Finally, when increasing from 500 to 550 W, a new displacement of the maximum intensity peak associated to the increase of the residual stresses caused by high ion bombardment corresponding to a high power on the Si_3N_4 target is presented. Thus, it was possible to determine that the coating deposited with 500 W presents lower residual stresses, which will directly influence better surface and mechanical properties, as corroborated in Figs. 6 and 9 [26–30].

The influence of the applied power on the residual stresses are observed in the Fig. 2, showing the relation of lattice parameter for the coatings obtained as a function of the applied power; so the lattice parameters were calculated by Eqs. (2) and (3), respectively, where the values 2θ were obtained from the plane of maximum intensity (200). In addition, the position where the material is stress-free $\left(a_0 = 4.3102 \overset{\circ}{A} \right)$ obtained from the interna-tional index files is indicated. These results showed that the 500-W coating presented a lattice parameter much closer to the stress-free position, indicating that this structure presented a lower amount of residual stresses compared to the other coatings [31–33].

$$n\lambda = 2d\,sen\theta \tag{2}$$

$$d = \frac{\alpha_0}{\sqrt{h^2 + k^2 + l^2}} \tag{3}$$

3.2 X-ray photoelectron spectroscopy (XPS)

In Fig. 3, XPS survey spectra for the TiSiCN coating are presented in relation to the applied power variation on the Si_3N_4 target. So, for the XPS analysis, the binding energy scale was referenced by using the work function method; in this sense, the literature is possible to find that the C 1s peak corresponding to C single bond C/C single bond H bonds of adventitious carbon (AdC), present on a majority of air-exposed samples such as Ti-Si-C-N composite, is most commonly employed for this purpose, irrespective of whether samples are electrically conducting or not. In this research in agreements with the Jesuraj and co-workers [29, 33, 34], the C 1s peak is closely correlated to the sample work function, such that the sum is constant, indicating that the electronic levels of the AdC layer align to the vacuum level, rather than to the Fermi level as commonly assumed. In the current research, this phenomenon can be understood given that the AdC layer is not an inherent part of the analyzed sample and that the interaction to
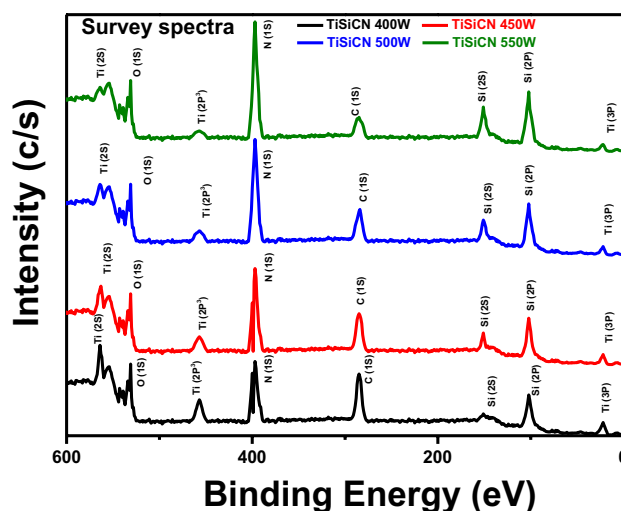

Fig. 2 Lattice parameter for TiSiCN as a function of applied power

Fig. 3 XPS spectra for TiSiCN coating with different applied power on Si_3N_4 target

the substrate is weak, showing in that a common Fermi level is not established at the interface. Thus, a straightforward complementary measurement enables using the C 1s peak of AdC present in the Ti-Si-C-N composite, for the purpose of BE-scale calibration for samples exhibiting decent electrical conductivity such as is shown in Table 2. This new practice resolves problems associated with the conventional method and allows for more reliable bonding assignments. Taking into account the last discussion, the work function ϕ_{SA} for the carbonitride samples (Ti-Si-C-N) was 4.85 eV [34–36].

From these spectra, the bonds present in the survey spectra can be analyzed. In this sense, intensity maxima (peaks) attributed to the signals of O 1s, Ti 2p3/2, N 1s, C 1s, and Si 2p corresponding to the binding energies 532.51 eV, 460.98 eV, 395.41 eV, 284.73 eV, and 100.12 eV, respectively. Therefore, through XPS spectrums for all the coatings, it was possible to establish the stoichiometry and the variation of the elements present as a function of the applied power as shown in Table 2 [23, 24]. In this sense in Table 2, the stoichiometric ratio (Ti/Si+N) was evidenced in relation to constituting TiN ad Si_3N_4 phases. Thus, sense was observed one reduction of stoichiometric ratio when the Ti content was decreased and the Si and N contents were increased; therefore, all TiSiCN coatings were sub-stoichiometric when the applied power was increased from 400 to 550 W.

For a more detailed study of the bonds present in the obtained coatings, Fig. 4 shows the high-resolution spectra for the C 1s, N 1s, Si 2p, and Ti 2p3/2 signals with the respective deconvolutions to determine the internal signals. Figure 4a shows the high-intensity spectrum for the C 1s, so in agreements with the Greczynski and co-workers [23, 34, 35], the chemical state analysis in X-ray photoelectron spectroscopy (XPS) relies on assigning well-defined binding energy values to core-level electrons originating from atoms in particular bonding configurations. Taking into account the above, the signal C(1s) was fitted by three internal Gaussian functions attributed to C-Ti, C-Si, and C-N bonds in agreement with the binding energies 281.52 eV, 282.64 eV, and 285.73 eV, respectively, as corroborated in the literature [16, 30–32]. The assignment of the BE value for the carbon signal

(C 1s) form Ti-Si-C-N material was performed taking into account the calibration of the chemical identity of AdC, due to that a most disturbing consequence of the BE referencing problems outlined above is the fact that the reported binding energies for primary core levels of constituent elements in many technologically relevant materials exhibit an unacceptably large spread, which often exceeds the magnitude of related chemical shifts [16]. Then, the corrected peak position measurements also show that, independent of material system, E^F_B of the C 1s peak is closely correlated to the sample work function Φ_{SA}, such that the sum $E^F_B+\Phi_{SA}$ is constant, indicating that the electronic levels of the AdC layer align to the vacuum level, rather than to the Fermi level as commonly assumed [37].

Figure 4b presents the high-intensity spectrum that corresponds to the N(1s) signal, which was fitted by two Gaussian functions attributed to the N-Ti, N-C, and N-Si bonds located at the binding energies 395.24 eV, 398.52 eV, and 392.21 eV respectively, as shown in the literature [37–41].

Figure 4c shows the high-intensity spectrum for the Si 2p signal. Therefore, the Si 2p signal was fitted by two Gaussian signals; the first one was attributed to Si-C bonds corresponding to Si in nanocrystallites of Ti-Si-C-N with the corresponding binding energy of 100.12 eV, and the second one was attributed to Si-C bonds corresponding to Si in the amorphous phase of the Si-C-N with the corresponding binding energy of 98.87 eV as corroborated in previous studies [32–34]. In this sense, in the Si 2p signal, it was not fitted with three separate peaks corresponding to Si-Ti, Si-N, and Si-C because it would suggest that Si atoms exist in three different chemical states. Finally, Fig. 4d shows the high-intensity spectra for the Ti 2p3/2 signal; this signal was fitted by one Gaussian signal attributed to Ti-C bonds corresponding to the binding energy of 460.98 eV, according to the literature [38–40]. Therefore, in the Ti 2p3/2 signal, it was not fitted with three separate peaks corresponding to Ti-Si, Ti-N, and Ti-C because it would suggest that Ti atoms exist in three different chemical states, which did not happen in this case.

Figure 4e presents the high-intensity spectrum that corresponds to the O 1s signal, which was fitted by one Gaussian

Table 2 Work function Φ_{SA} for the (TiSiCN) sample, corrected peak position E^F_B, and shift by ΦSA calibration for the C 1s, N 1s, Si 2p, Ti 2p3/2, and O 1s signals

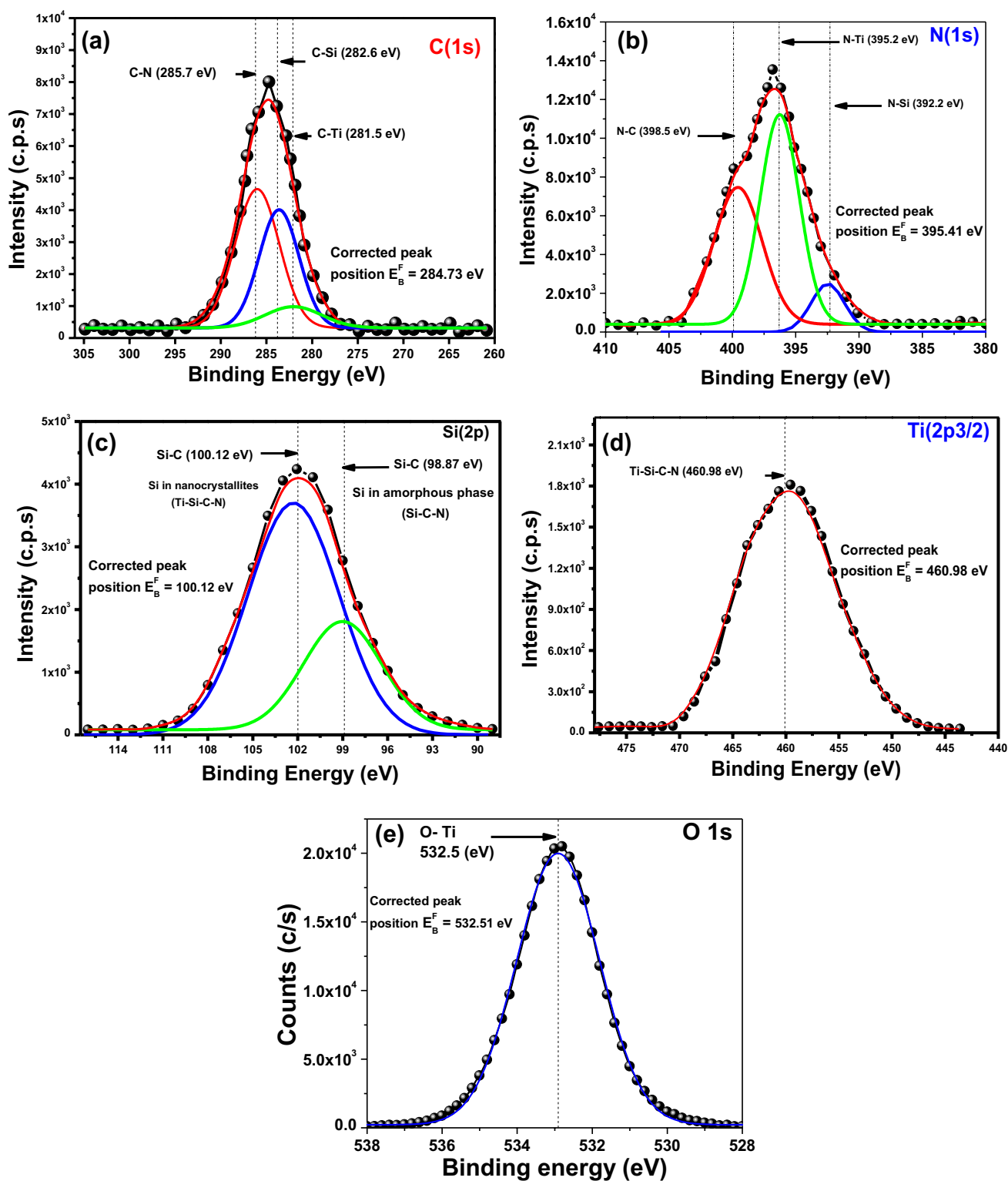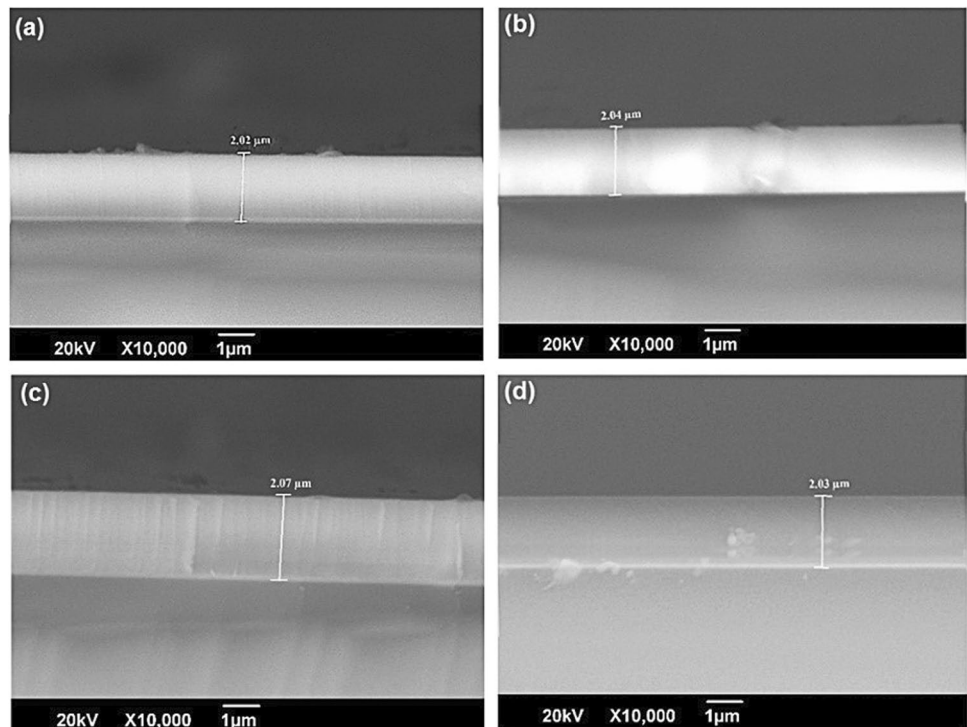| Signal	Initial position signal (eV)	Work function Φ_{SA} (eV) (TiSiCN) sample	Corrected peak position E^F_B (eV)	Shift by Φ_{SA} calibration (eV)
C 1s	289.58	4.85	284.73	4.85
N 1s	400.26	4.85	395.41	4.85
Si 2p	104.97	4.85	100.12	4.85
Ti 2p3/2	485.63	4.85	460.98	4.85
O 1s	537.36	4.85	532.51	4.85

Fig. 4 XPS high-resolution spectrum for **a** C 1s, **b** N 1s, **c** Si 2p, **d** Ti 2p3, and O 1s signals

Table 3 Variation of the atomic content and stoichiometric ratio in the TiSiCN coatings in relation to the applied power on Si_3N_4 target

Power (W) (Si_3N_4 target)	Atomic content (%)				Stoichiometric ratio (Ti/Si+N)
	Ti	Si	C	N	
400	0.25	0.45	0.12	0.18	0.39
450	0.20	0.50	0.13	0.19	0.29
500	0.17	0.53	0.09	0.21	0.23
550	0.15	0.55	0.07	0.23	0.19
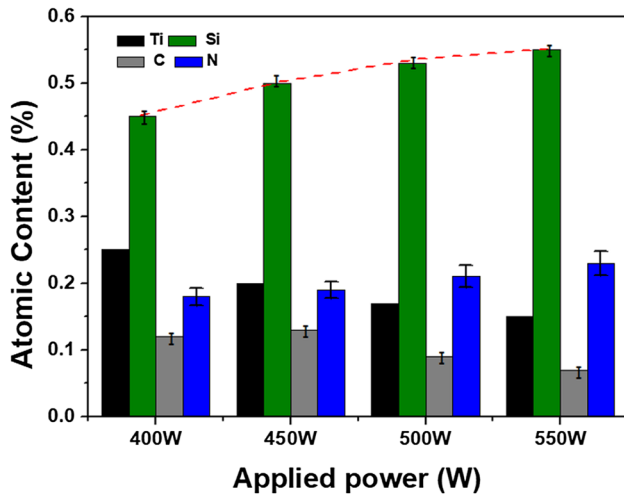
Fig. 5 Atomic content variation in the TiSiCN layers in relation to the power applied to the Si_3N_4 target

function attributed to the O-Ti bonds located at the binding energies 532.51 eV, as shown in the literature [38, 39]. So, the presence of oxygen can be attributed to surface contamination phenomena of the sample and to the coating processing associated with the oxygen present in the sample which comes from the oxidation of the Ti target.

Taking into account Fig. 3 and Table 3, Fig. 5 shows a decrease in the intensity of the Ti and C peaks and an increase in the Si and N peaks, evidencing a variation of the species present in the plasma and an increase in the Si and N content within the TiSiCN coatings. This increase in the Si and N content is attributed to an increase in the applied power to the Si_3N_4 target, which causes a higher intensity and density of the bombardment of Ar^+ atoms with a higher kinetic energy to impact the target surface. Thus, a higher amount of Si and N sputtered particles is generated, which will be deposited on the surface of the substrate (HSS steel and silicon). This increase of the bombardment intensity and a higher amount of sputtered particles will influence the morphological, mechanical, and tribological properties as a corroborated in Figs. 8, 10, and 12, respectively [42]. On the other hand, the presence of the O 1s signal is attributed to environmental contamination of the coating; some authors such as Li et al [38] have synthesized this quaternary TiSiCN coating by other methods obtaining similar bonds to those obtained in this research [38. 39].

Fig. 6 SEM micrographs of the cross-section for individual TiSiCN layers as a function of applied power: **a** TiSiCN (400 W), **b** TiSiCN (450 W), **c** TiSiCN (500 W), and **d** TiSiCN (550 W)

3.3 Scanning electron microscopy by SEM and EDX study

Figure 6 shows the SEM micrograph of the cross-section of TiSiCN coatings as a function of the applied power on the Si_3N_4 target, deposited on silicon substrates. In that sense, it is important to highlight that the time correction in relation to the applied power was performed to ensure similar thicknesses for all coatings. Therefore, in all the SEM micrographs, the approximate thicknesses of 2 ± 0.03 μm were determined. In addition, in the SEM micrographs, a partial columnar growth could be observed in all the coatings and that is much more evident for the coatings deposited with 500 W, since this coating presented a lower amount of residual stresses during the deposition process, which generates a more ordered growth favoring the columnar growth, causing a more homogeneous coating with a lower roughness and smaller grain size, as corroborated previously. On the other hand, the gray-scale difference for the micrographs is associated with a change in elemental composition between the Si substrate and the quaternary TiSiCN coating. So, for the TiSiCN coating, a brighter contrast is observed, and for the silicon substrate, a darker contrast is observed; this change in pitch occurs due to the electron density of the materials. Additionally, the partial columnar growth can be attributed to the elevated ionic attack of Ar+ atoms on the layers that was applied during the deposition process, thus generating a highly dense cross-section.

Figure 7 shows a compositional analysis by EDX on the cross-section of the coating (Fig. 7(a)) in order to differentiate and evidenced between the deposited coating (TiSiCN), which is corroborated by the EDX spectrum (Fig. 7(b)), where peaks attributed to Ti, Si, C, and N. And, the EDX spectrum (Fig. 7(c)) of the substrate, where the presence of Si (silicon 100) and oxygen is due to a partial oxidation of the substrate, was evidenced.

3.4 Transmission electron microscopy (TEM)

Figure 8a shows the HR-TEM micrographs of a nanocomposite coating recorded in cross-sectional configuration. The absence of diffraction contrast in much of these HR-TEM images indicates that the coating is mainly constituted by an amorphous matrix, which can be associated with the continuous a-SiCN composite [43, 44]. The formation of a halo ring in a fast Fourier transformed (FFT) image certifies the amorphous character of the coating. However, we achieve detecting small regions that exhibit a noisy diffraction contrast due to presence of nanocrystals that should correspond to the nc-TiSiCN system. According to the HR-TEM image
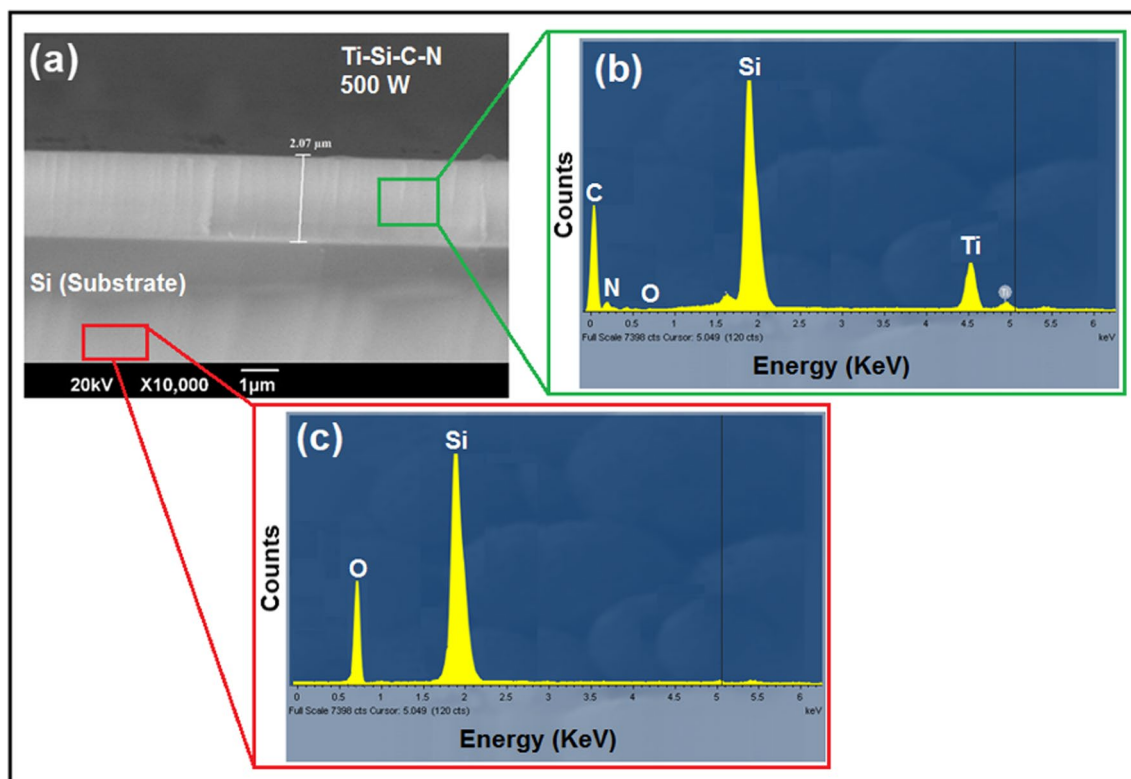

Fig. 7 Compositional study on the cross-section of TiSiCN coating deposited with 500 W. (a) Cross-sectional SEM, (b) EDX analysis for TiSiCN coating, and (c) EDX analysis for substrate

Fig. 8 TEM images of the cross-section for the individual TiSiCN layer deposited with 500 W: **a** HRTEM exposing the nc-TiSiCN crystal and the amorphous area of the a-SiCN matrix and **b** nanocomposite configuration with nc-TiSiCN crystals and a-SiCN amorphous matrix
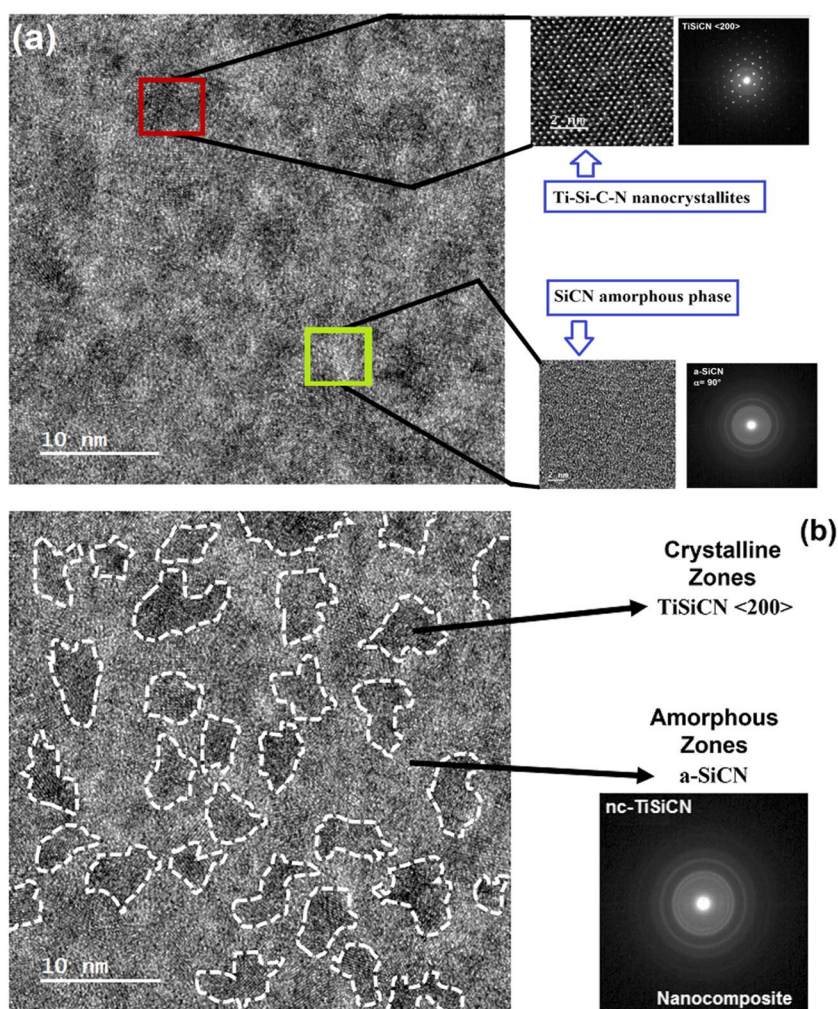
shown in Fig. 8b, the nc-TiSiCN nanocrystals have an irregular shape, with an average size of around 6 nm, and they are dispersed along the amorphous matrix. Thus, the TEM allowed resolving the expected nanocomposite system and confirmed quite precisely by the previously designed nominal configurations (associated with deposition conditions). The amorphous nature of the coating is linked to the use of a deposition temperature; due to that, this phenomenon is attributed to the mobility of the atoms in the plasma on the surface material, which favors the position of minimum energy that increases diffusivity and grain size in agreement with the literature [25–28]. Thus, in the crystalline zone corresponding to the nanocrystal, the crystalline plane in the direction (200) can be observed, referring to nc-TiSiCN, as evidenced by XRD analysis (Fig. 1). Therefore, in the quaternary phases of the nanocomposite obtained by XRD, it can be suggested that in the solid solutions, the Ti and Si atoms are in coordinates (0,0,0); on the other hand, the C and N are located in coordinates (1/2,1/2,1/2), simulating a NaCl-type structure. Furthermore, the XRD (200) peak widened; as a result, a nanograined microstructure is

produced in solid solution. This research was categorized a refinement structural system for TiSiCN with the interplanar distance of $d_{(200)} = 2.1395$ Å in agreement with the literature [25–28], so in the quaternary material, the intensity of the (200) plane indicates that Wyckoff 4b sites are occupied by C and N atoms and Wyckoff 4a sites are occupied by Ti and Si atoms randomly. Moreover, the interface between the amorphous zone of the matrix and the nanocrystal is denoted in Fig. 7(b); therefore, the number of nanocrystals and geometric configuration defines the variation of the mechanical properties such as shown via TEM results.

On the other hand, taking into account the high vacuum conditions in the processing of the coatings, it can be observed from the XPS results that the oxygen (O) content is very low, but there is presence of this element; therefore, it is possible that O has been added at the grain boundaries or modified at the stoichiometry of the TiN and Si_3N_4 phases; however, no strong evidence of significant phase modification was witnessed in the XRD results. Then, considering the above, as well as the XPS results, the cross-sectional EDS results reveal a low oxygen contribution,
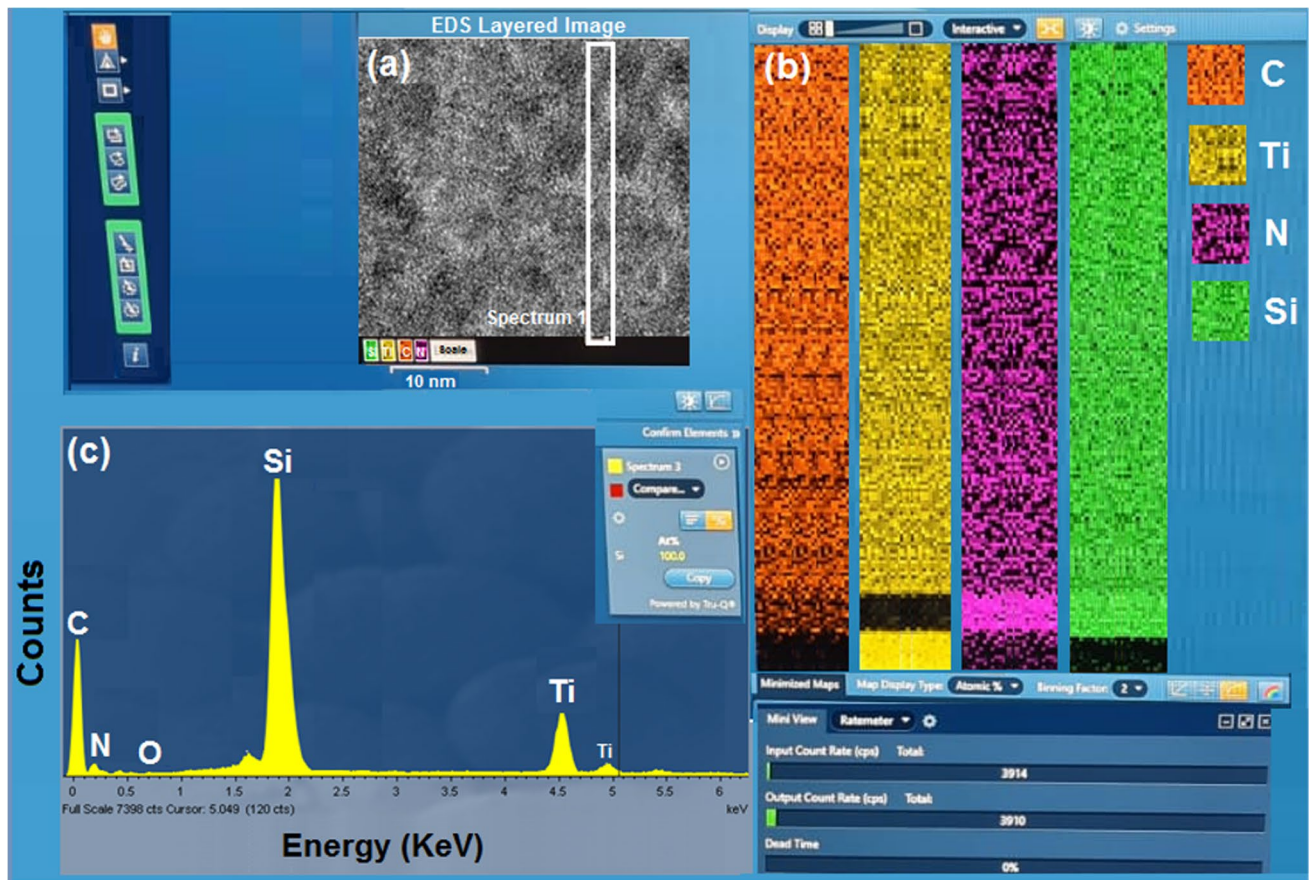
Fig. 9 Compositional analysis: **a** TEM-EDX image, **b** distribution of the elements present, and **c** spectrum EDS

which may affect the stoichiometry of the grain boundaries in the nanocomposite, since the grain boundaries are symmetry breaking zones where O can interact with the phase and adjust with the amorphous nature of a-SiCN as observed in the TEM results.

3.4.1 Elemental composition for TEM-EDX analysis

Figure 9 shows the results obtained by TEM-EDX in order to determine the distribution of elements present in the coating. Figure 9a shows the surface EDX image of the coating obtained with 500 W, where a zone (spectrum 1) was evidenced, in which several spectra were taken for a statistical analysis of the elements present. Figure 9b shows a composition map associated to the atomic distribution of the elements present in the TiSiCN coating, where different colorations attributed to each of the elements (Ti, Si, C, and N) were evidenced. Finally, Fig. 9c shows the EDX spectrum obtained, which shows the presence of peaks corresponding to Ti, Si, C, and N. In addition, a low-intensity peak corresponding to O was evidenced, which is associated to the oxidation of the substrate (silicon 100).

3.5 Surface characterization

3.5.1 Atomic force microscopy

The morphology of the nc-TiSiCN coatings for the different applied powers was analyzed by AFM. The analyzed area in Fig. 10 for all samples was 50 µm × 50 µm with a Z scale around 5 µm, the analyzed coatings were synthesized on silicon (100) substrates and as a result of the analysis were obtained images in a non-contact mode in two dimensions, and based on the micrographs, the results of roughness and grain size were obtained, supported statistically in the program (SPIP®). In the AFM images for the individual layers, it was possible to determine that all the coatings presented circular grain morphology with a tendency to reduce as the power applied to the Si_3N_4 target is increased. On the other hand, a more homogeneous morphology could be observed on the nc-TiSiCN layer surface deposited at 500 W about the other layers. The morphology changes can be explained by the effect of ion bombardment of Ar+ atoms on the Si_3N_4 target, which increases the energy of the spacing present in the plasma, and these spices are directed to the surface of the substrate with higher energy. In this sense, the surface

Fig. 10 Atomic force micros-
copy (AFM) images for
individual TiSiCN layers as a
function of the applied power: **a**
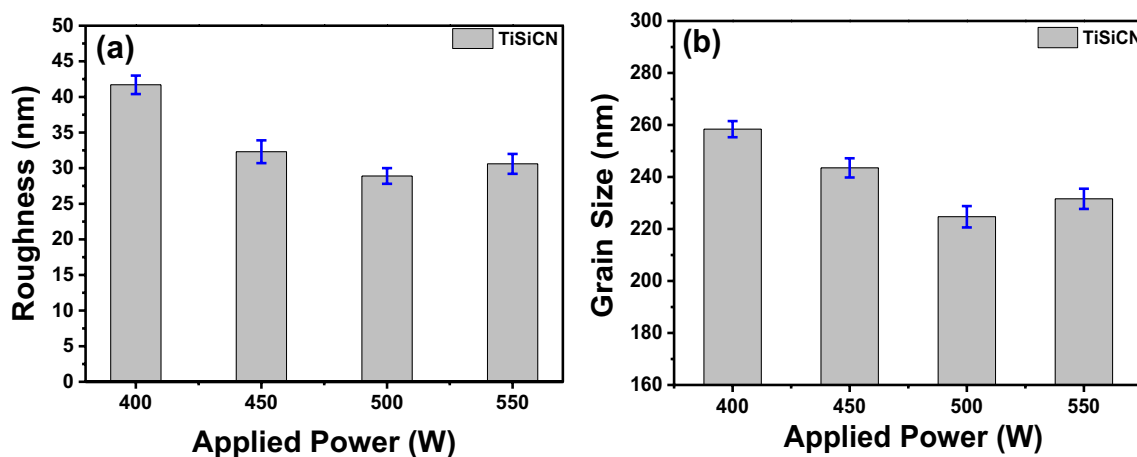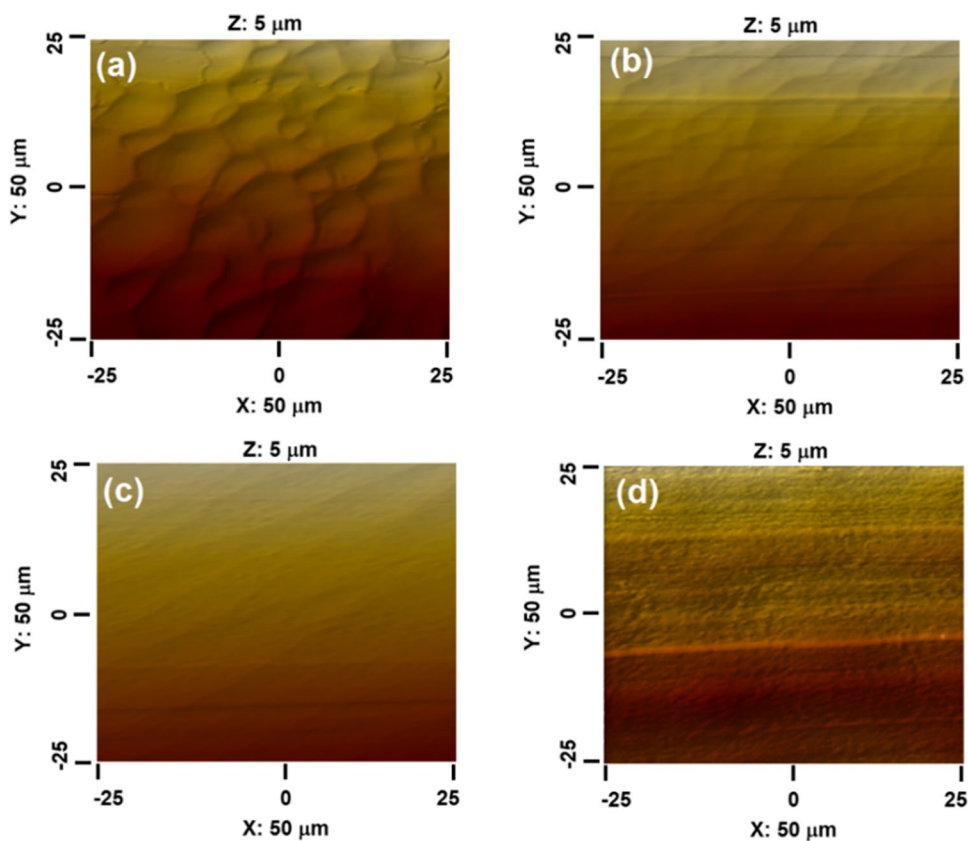400 W, **b** 450 W, **c** 500 W, and
d 550 W

Fig. 11 Influence of applied power on the morphology of TiSiCN coatings: **a** roughness vs. applied power and **b** grain size vs. applied power

of the layers is modified as an effect of the bombardment, due to the increase in the atomic energy absorbed on the substrate, causing nucleation points and causing a decrease in grain size. However, when applying a power higher than 550 W to the Si_3N_4 target, an increase of roughness and grain size is observed again, which may be associated to an excessive energy input corresponding to the re-sputtering phenomenon [27, 39].

Figure 11a and b present the analysis of roughness and grain size, respectively, for all coatings as a function of the power applied to the Si_3N_4 target. In Fig. 11a and b, it was determined that increasing the applied power from 400 to 500 W presented a decrease of 30.7% and 13.1% for roughness and grain size, respectively. Subsequently, when increasing the applied power from 500 to 550 W, an increase of 5.6% and 2.9% was observed for roughness and grain size,

respectively. This behavior in the surface properties is attributed to the residual stresses as shown in Fig. 1b, where it was possible to determine the residual stresses in comparison to the other coatings, and by increasing again the applied power from 500 to 550 W, it was possible to evidence again the presence of residual stresses within the crystalline structure. Finally, by means of this superficial analysis, it was determined that the coating deposited with 500 W presented a lower amount of residual stresses (Fig. 1b), which generates a more orderly and regular growth, obtaining a denser structure and causing a decrease in surface roughness, as well as a much smaller grain size. Taking into account the above, it was thus determined that the surface of the TiSiCN coating deposited with 500 W presents a higher amount of grains in the analysis area, thus generating a higher grain edge density, being these grain edges obstacles or impediments to the movement of dislocations, which may influence the physical properties of the material. Therefore, these morphological characteristics affect the mechanical and tribological properties in the nc-TiSiCN system [45, 46].

3.6 Mechanical properties

The load-depth curves obtained from the nanoindentation test can be seen in Fig. 12 for the different coatings. Figure 13 shows the mechanical behavior of the surfaces, evidencing that the TiSiCN coating deposited at 500 W presents a reduction in depth of 23.5% in relation to the TiSiCN coating deposited at 400 W, a reduction of 18.9% in relation to the TiSiCN coting deposited at 450 W, and 12.8% in relation to the TiSiCN coting deposited at 550 W. This behavior can be explained by properties such as hardness which increases the resistance of the material to be penetrated. Therefore, the mechanical properties such as hardness (H) and elastic modulus (E) were analyzed by the Oliver and Pharr method presented in Fig. 13a and b, respectively [45]. The increased mechanical properties can be related to morphology, size, and quantity of the nc-TiSiCN nanocrystals observed by TEM (Fig. 8). In that sense, the nanocrystal character restricts the dislocation movement, modifying the amount of the amorphous phase; this phenomenon has been reported by Wang et al. [41], for the same material deposited at 500 W [41, 47]. Finally, it was possible to observe the evolution in the mechanical properties as function of preparation conditions in the coatings, in agreements of Zheng and co-workers [48].

Figure 13a and b show the results of hardness (H) and reduced elastic modulus (E_r) for all coatings deposited on silicon (100) substrate as a function of the applied power on the Si$_3$N$_4$ target. In this research, it could be determined that the nc-TiSiCN coating deposited at 500 W presents a higher resistance to be indented compared to nc-TiSiCN coatings deposited at powers of 400 W, 450 W, and 550
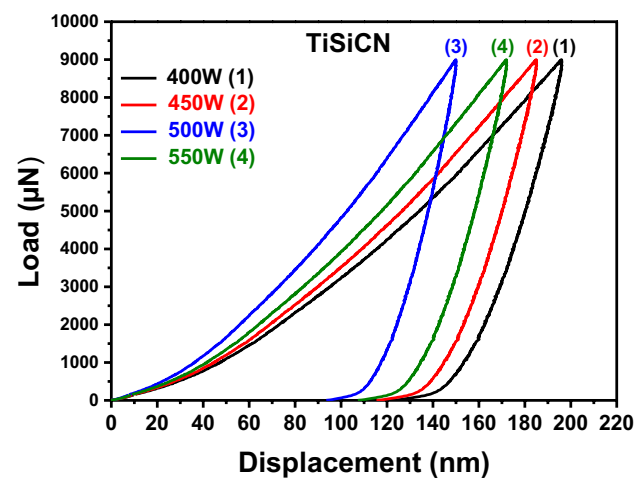

Fig. 12 Load-depth curves for individual nc-TiSiCN layers as a function of applied power

W, respectively. This behavior can be attributed to factors such as the characteristics of the nc-TiSiCN nanocrystals observed by TEM (Fig. 8) and a smaller grain size, as observed in the AFM results (Fig. 11); since it presents a greater amount of nanocrystals with less irregular morphologies and greater amount of grain edges, these edges act as impediments or obstacles to the sliding of the dislocations, so a greater amount of energy will be required to overcome these obstacles [25, 40]. In addition, the compressive stress relief generated during the deposition process when the applied power was increased can contribute to the increase of the hardness for the 500 W and such as observed from X-ray results (Fig. 1b). So, the nc-TiSiCN coating deposited with 500 W presents better mechanical properties such as hardness (H) and reduced elastic modulus (E_r).

From the nanoindentation results, the resistance to plastic deformation (H^3/E^2) and the elastic recovery (R) were determined as a function of the applied power on the Si$_3$N$_4$ target. The elastic recovery of the coatings was calculated using the following equation [48, 49]:

$$R = \frac{\delta_{\max} - \delta_{\mathrm{p}}}{\delta_{\max}} \tag{4}$$

where $\delta_{\max}$ is the maximum displacement and δ_{P} is the residual displacement. The data for Eq. (4) were taken from the load-depth curves presented in Fig. 12. Figure 14a and b show the values obtained for the plastic deformation resistance (H^3/E^2) and elastic recovery (R) for the different coatings, which determined that the highest plastic deformation resistance (H^3/E^2) and elastic recovery (R) were obtained for the nc-TiSiCN coating deposited at a power of 500 W, which is mainly due to factors such as the characteristics of the nc-TiSiCN nanocrystals observed by TEM (Fig. 8) and their mechanical properties such
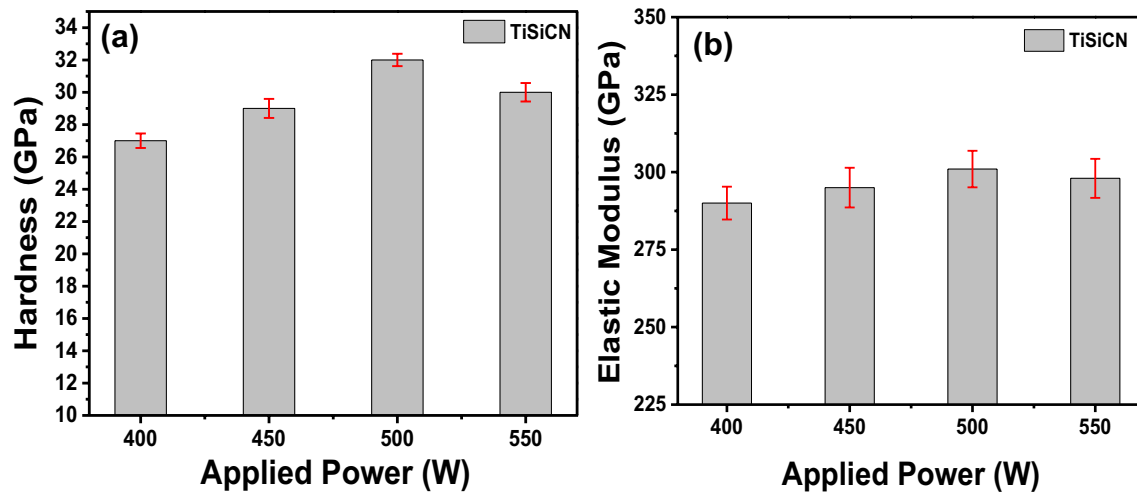
Fig. 13 Mechanical properties of the nc-TiSiCN layer as a function of the applied power on the Si_3N_4 target: **a** hardness and **b** elastic modulus
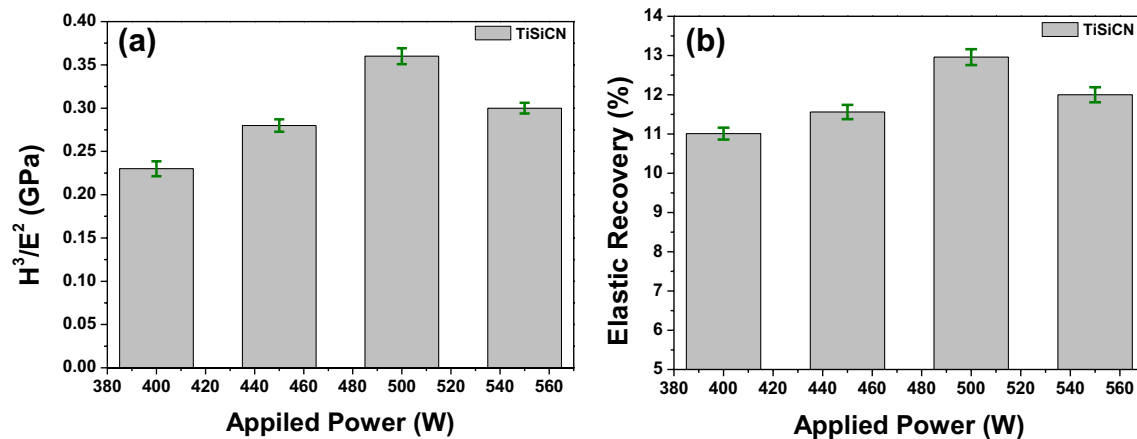

Fig. 14 Mechanical properties of the coatings as a function of the applied power on the Si_3N_4 target: **a** plastic deformation resistance (H^3/E^2) and **b** elastic recovery ($\%R$)

as hardness and reduced elastic modulus, which is analyzed in Fig. 13. Finally, it was possible to observed that the generation of a continuous amorphous a-SiCN phase and a discrete nc-TiSiCN phase, with fusiform grain morphology where inhabiting the crystalline phase observed by TEM, was responsible for an increase in the mechanical properties such as hardness from 27 to 32 GPa and elastic modulus from 290 to 301 GPa which was evidenced.

3.7 Tribological properties

Figure 15a presents the friction coefficient in the dry environment of the interaction between steel counterpart (100Cr6) and the surface of nc-TiSiCN coatings deposited on an HSS steel substrate at different powers. The friction coefficient results in dry environment presented two

characteristic stages, typically occurring during the pin-on-disc test. Stage I, known as the start-up period, is associated with the interferential friction mechanism, due to the contact of the asperities and the counterpart (100Cr6 steel pin), in which the reduction of the asperities occurs, leading to the formation of wear particles or debris [45]. These particles on the surface generate a rapid increase in the friction coefficient followed by a slight decrease until it stabilizes. In stage II, the settling (running-in) period occurs in which the reduction of these asperities is maintained together with the appearance of new defects in the coating that lead to a friction coefficient stabilization [49].

Taking into account the above, Fig. 15b shows the friction coefficient value in the dry environment as a function different nc-TiSiCN coatings obtained with different applied powers on the Si_3N_4 target. This behavior is related
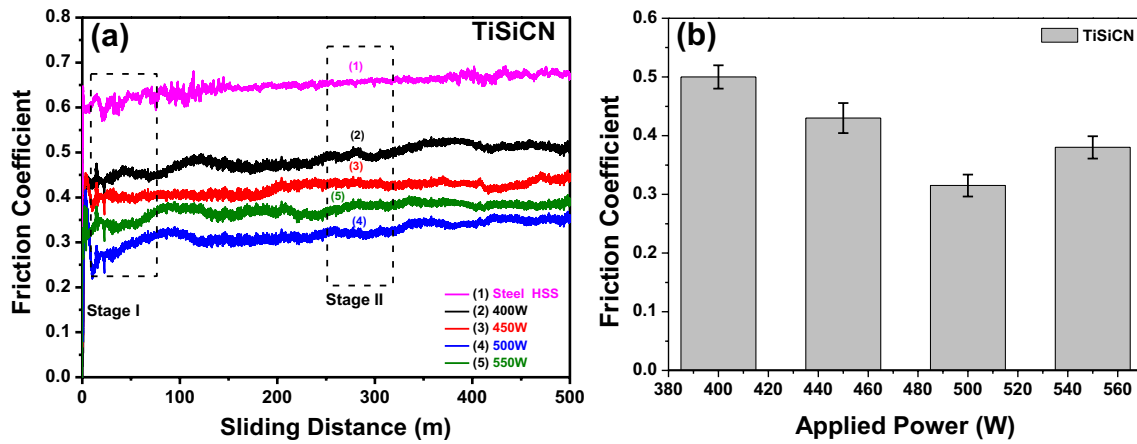
Fig. 15 Tribological properties of TiSiCN coatings deposited with different powers of 400 W, 450 W, 500 W, and 550 W, in dry environment: **a** friction coefficient as a function of sliding distance from pin-on-disc test and **b** friction coefficient as a function of applied power

to the friction model proposed by Archard [50]. This correlates the mechanical (H, E_r) and morphological (roughness) properties of the coatings as presented in Eq. (5), where it is indicated that the surfaces with better mechanical properties and lower roughness, as is the case of the TiSiCN coating deposited at 500 W, presented a lower friction coefficient, as proved in the tribological test, since this surface can withstand a greater continuous passage of the counterpart with the uncoated steel substrate and the other nc-TiSiCN coatings obtained with powers of 400 W, 450 W, and 550 W, respectively; thus, the nc-TiSiCN coating deposited at 500 W presented a lower wear rate in the analyzed surface.

$$\mu = \frac{F_f}{F_n} = C_k \frac{R_{(s,a)}}{\sigma t_{(H,E_r)}} \qquad (5)$$

where μ is the friction coefficient of the system, C_k is a fit constant that depends on the test conditions, $R_{(s,a)}$ is the roughness of the coating which can be quadratic or arithmetic, and $\sigma t_{(H,E_r)}$ is a variable that depends on the mechanical properties of the system such as hardness (H) or elastic modulus (E_r).

Figure 16 presents SEM micrographs for all wear surfaces of nc-TiSiCN coatings deposited on HSS steels in a dry environment as a function of applied power. The SEM micrographs were used to determine the mechanisms present on worn surfaces after performing the pin-on-disc test. In the SEM micrographs, it was possible to observe the wear abrasive generated by penetration and fracture of the asperities by the continuous passage of the counterpart over the surface, generating hardened abrasive particles due to plastic deformation. These particles adhered to both surfaces in the tribological pair (counterpart-coating) generating a plowing and wear mechanism on that surface. It

was also possible to observe the adhesive wear which was produced in certain areas of the counterpart (pin 100Cr6) plastically deformed and adhered to the nc-TiSiCN coating surface after withstanding the external load exerted on the counterpart.

In the SEM micrographs of the wear tracks produced in the tribological test, it could be seen that for the uncoated HSS steel substrate (Fig. 16a), the predominant surface wear mechanisms are abrasive and adhesive. This is due to its low mechanical properties and a relatively high friction coefficient compared to the TiSiCN coating, which produces a large number of particles on the surface that are deformed and hardened by plastic deformation. In addition, the constant passage of the counterpart removes and deforms the asperities associated with the roughness of the HSS steel, so that the contact area increases and the number of wear particles decreases. Subsequently, this increase in the contact area generates micro-welds, which are detached during the tribological test and produce a removal of material [45, 49–52]. On the surfaces of steels coated with TiSiCN in a dry environment (Fig. 16b, c, d, and e), it was determined that the predominant wear mechanisms on these surfaces were adhesion and abrasion although more reduced with the uncoated steel; this change of behavior to the HSS steel substrate is due to the change of the mechanical properties of surfaces and surface morphologies in the coatings which provide a greater resistance to be deformed, generating a lower amount of removal and wear of the material, where in the TiSiCN coating deposited with an applied power of 500 W, a lower wear track was found.

The 3D profiles of all the wear tracks obtained by profilometry are shown in Fig. 17; in that sense, the profilometry results corroborate the wear analysis associated to wear tracks observed by SEM (Fig. 16a), for uncoated HSS steel substrate and for all nc-TiSiCN coatings deposited at
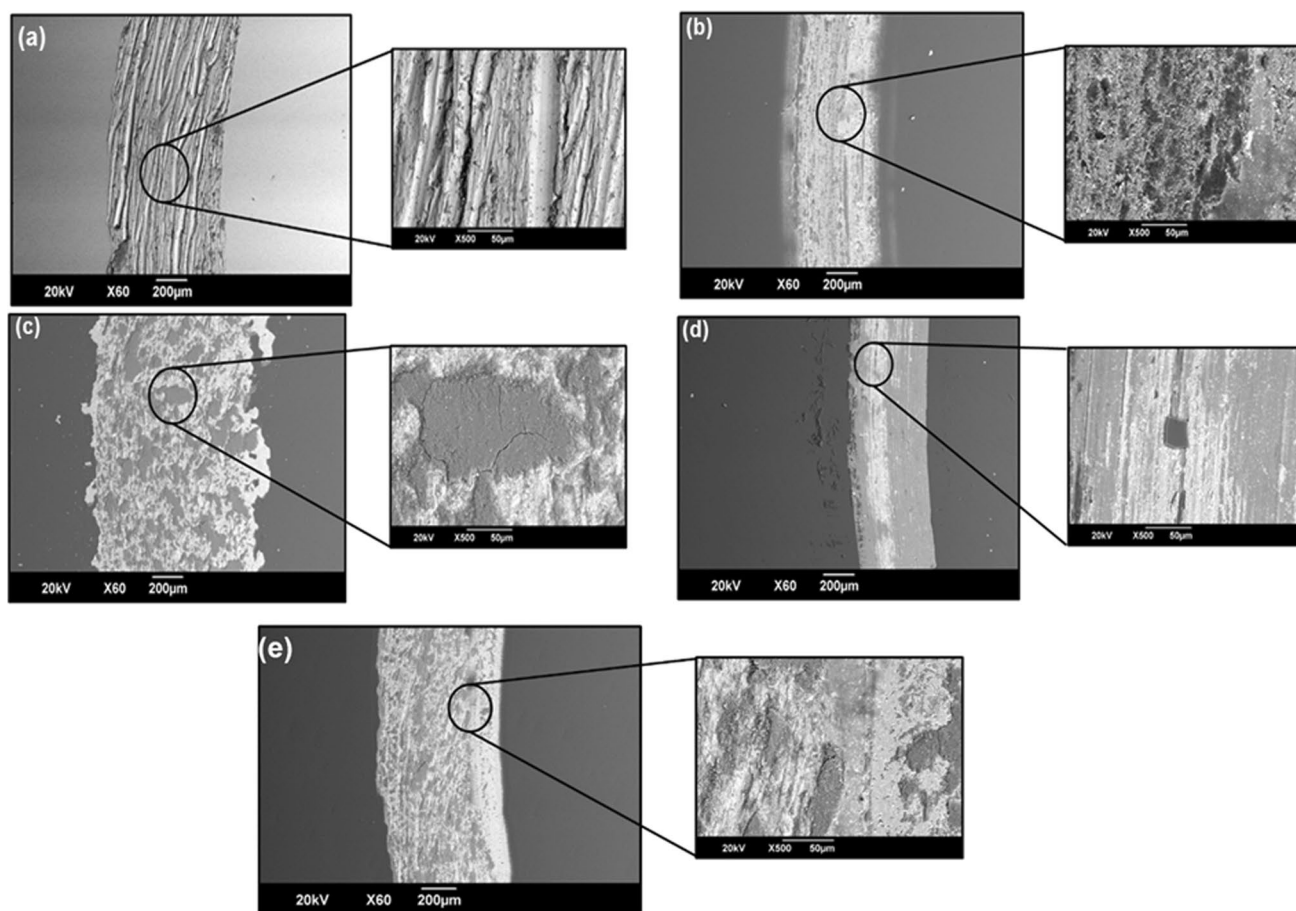
Fig. 16 SEM micrographs of the wear tracks of the TiSiCN coating as a function of the applied power on the Si$_3$N$_4$ target: **a** HSS steel, **b** 400 W, **c** 450 W, **d** 500 W, and **e** 550 W

different applied powers, such as 400 W, 450 W, 500 W, and 550 W. Considering the above, the profilometry images show that the nc-TiSiCN coating deposited with 500 W presents lower amplitude and penetration in the worn track. This wear behavior is due to the nanocomposite characteristics which are consisted of nc-TiSiCN nanocrystals and an amorphous a-SiCN matrix and the mechanical and morphological properties previously described, which minimize the deformation of the surface micro-irregularities affecting the contact area in the wear process, thus minimizing the volume removed from the coating as described in Fig. 16d.

3.8 Wear rate analysis

To determine the amount of wear produced during the tribological test in a dry environment, a quantification of the wear rate was made from the pin-on-disc test (Figs. 15 and 17). Taking into account the data obtained from the profilometry test, the wear rate was determined for all the dry environment surfaces obtained during the tribological test and calculated from Eq. (6) [53].

$$k = \frac{V}{F.s} \quad \text{and} \quad S = 2.\pi.r.n \quad (6)$$

where k is the wear rate, F is the applied force, V is the track volume, s is the perimeter of the wear track, n is the number of cycles or turns of the test, and r is the radius of the wear track cycles.

To satisfy the terms expressed in Eq. (5), it is necessary to determine the volume of the wear track; therefore, Fig. 18a and b shows the width and depth values from the wear track generated during the tribological test for TiSiCN individual coatings deposited as a function of the applied power (400 W, 450 W, 500 W, and 550 W). The results show a geometrical reduction in the wear tracks when the mechanical properties improve, such as the elastic modulus (Fig. 13) and the plastic deformation resistance (H^3/E^2) (Fig. 13), thus reducing the micro-crack production and minimizing delamination mechanisms. In that sense, the coatings obtained with lower power deposition (400 W) presented higher track width (1100 μm) and track depth (1.1 μm) values, compared to the TiSiCN coating
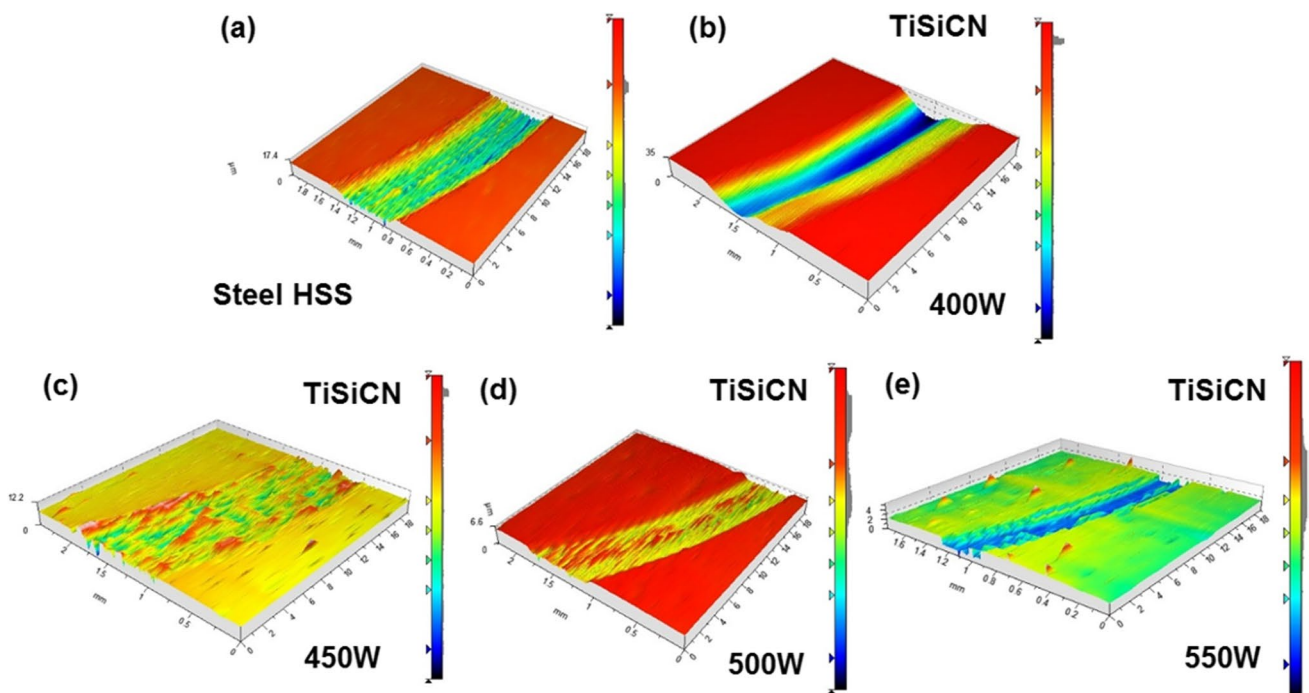
Fig. 17 3D profile images of the wear tracks of the nc-TiSiCN coating as a function of the applied power on the Si_3N_4 target: **a** HSS steel, **b** 400 W, **c** 450 W, **d** 500 W, and **e** 550 W
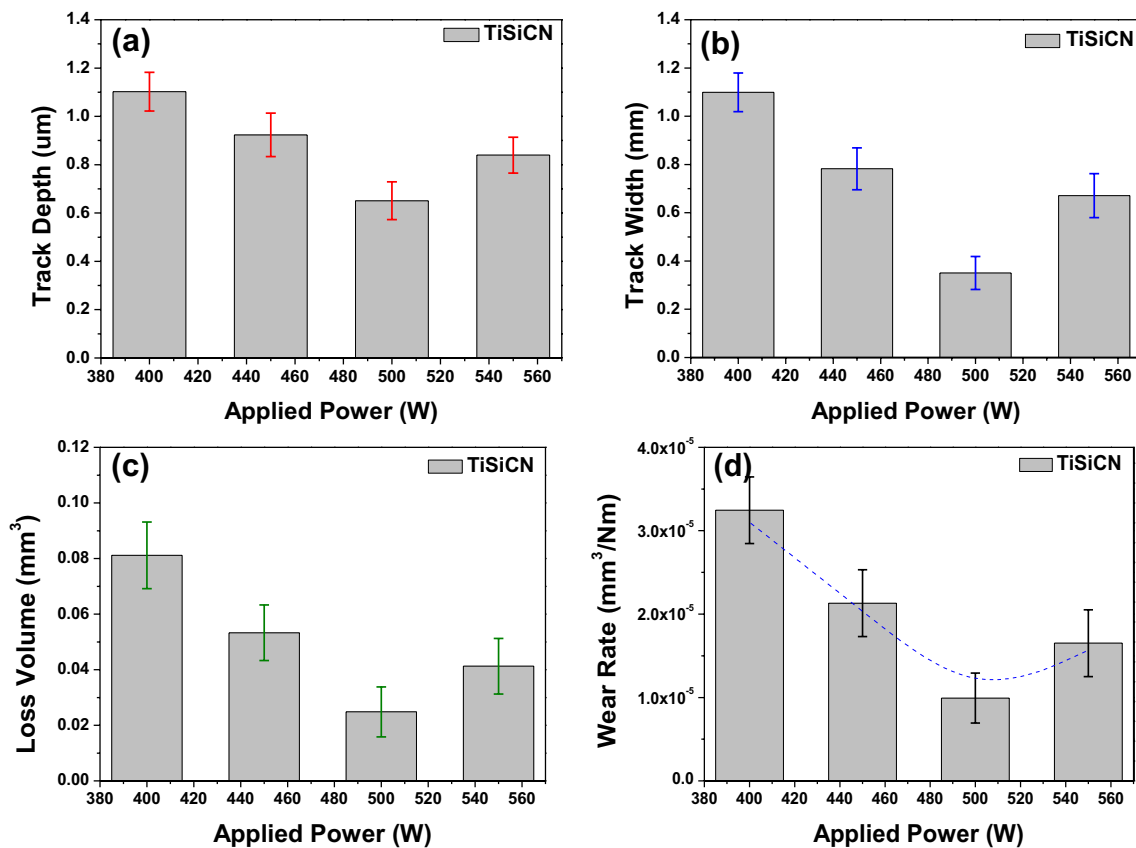

Fig. 18 Geometric measurements of wear tracks after pin-on-disc test for TiSiCN coatings deposited as a function of power applied on the Si_3N_4 target: **a** depth in the wear track, **b** width of the wear track, **c** volume lost, and **d** wear rate variation

deposited at 500 W, which presented lower track width (350 μm) and track depth (0.65 μm) values. Figure 18a and b present a reduction of 68% in the width and 40% in the depth values of the wear tracks concerning the coating obtained at 400 W. Taking the above into account, it can be determined that the wear rate results for uncoated steel substrate and all nc-TiSiCN coatings deposited as a function of the applied power on the Si_3N_4 target vary with the lost volume of each material. Therefore, in Fig. 18c the volume loss for the substrate and all coatings was determined taking into account the track width and the track depth results (Fig. 18a and b). So, Fig. 18c shows a significant reduction of the wear volume as a function of the applied power, which is consistent with the mechanical property evolution and of the friction coefficient reduction. In this sense, Fig. 18d shows a wear rate decreasing as a function of the applied power on the Si_3N_4 target and an increase for the nc-TiSiCN coating deposited at a power of 550 W. The maximum reduction of the wear rate corroborates that the nc-TiSiCN coating deposited at 500 W presented a higher wear resistance. This behavior was attributed to the nanostructural modification of the [nc-TiSiCN]-[a-SiCN] nanocomposite, the lubricating behavior that provides from carbon that can be caused by the formation of amorphous silicon carbon nitride and carbon in the form of graphite and is also related to the increase in mechanical properties, reduction of the friction coefficient, and the wear rate reduction [14, 38, 40].

3.9 Scratch test analysis

To determine the critical load at which the nc-TiSiCN nanocomposite coating can be delaminated from the substrate as a function of the adhesive properties, the scratch technique was used. Figure 19 shows the different test results in relation to the applied power on the Si_3N_4 target. The adhesion properties are characterized by two concepts; critical load, at which the cohesive failure occurs (L_{C1}), is the moment where the first cracks appear; on the other hand, there is the
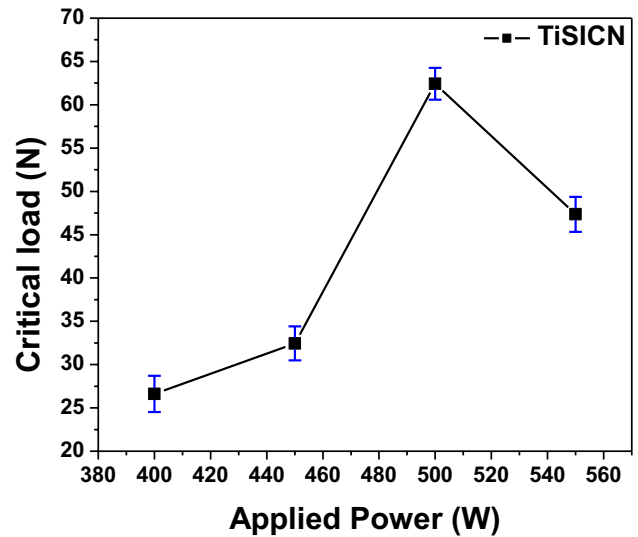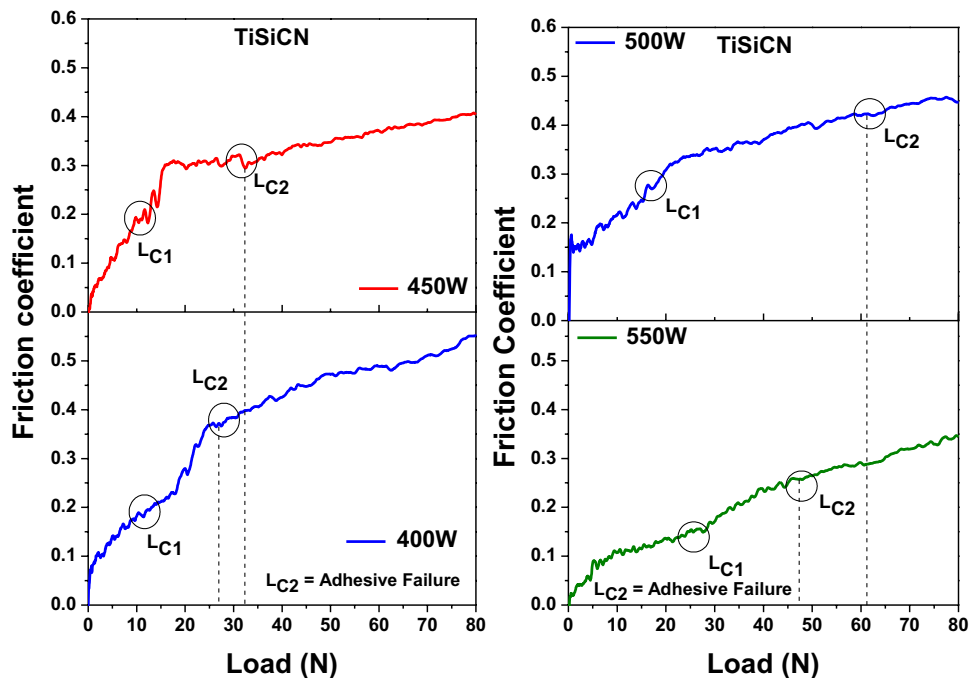

Fig. 20 Critical load for all nc-TiSiCN coatings deposited as a function of the applied power on the Si_3N_4 target

Fig. 19 Scratch test curve for all nc-TiSiCN coatings deposited as a function of applied power on the Si_3N_4 target

critical load at which the adhesive failure occurs (L_{C2}) and is related to the first delamination at the crack edge. So, the loads were found in the regions of the scratch curve where the friction coefficients were stabilized and the load becomes independent of friction. The first detected zone refers to the load at which cohesive failure occurs (L_{C1}), and the second stabilization zone refers to the load at which adhesive failure occurs (L_{C2}) [54, 56].

Figure 20 shows the increase of the critical load (L_{C2}) for all the nc-TiSiCN coatings deposited as a function of the applied power on the Si_3N_4 target. In Fig. 20, it can be analyzed that the coating deposited at 500 W presents the highest critical load at which the adhesive failure occurs, which indicates that the nc-TiSiCN coatings obtained with 500 W present better coating adhesion and less coating delamination, compared to the coatings obtained with 400 W, 450 W, and 550 W. In this sense, it can be analyzed that the layer grown with a power of 550 W shows a significant reduction in the scratch resistance (critical load), which can be attributed to the reduction of the mechanical and tribological properties evidenced above. However, a maximum critical load of 62.4 N was observed for the nc-TiSiCN coating obtained at 500 W, representing an increase of 57.4% in relation to the critical load for the coating grown at 400 W. This behavior is attributed to the characteristics of the [nc-TiSiCN]-[a-SiCN] nanocomposite structures found by XRD (Fig. 1) and TEM (Fig. 8) and also to the increase of mechanical properties determined by nanoindentation (Figs. 16 and 17) and tribological properties analyzed by pin-on-disc test (Fig. 17).

In this sense, the symmetry breaking in the amorphous crystalline interface of the nanocomposite together with the increase of the nanocrystal generation with the applied power produced an evolution in the tribological properties evidenced by friction coefficient decreasing in relation to uncoated HSS steel; in this sense, the nanocomposite obtained with a power of 500 W exhibited the best performance showing the lower friction coefficient of 0.31 and lower critical load of 62.4 N, with lower wear rate. Finally, it was possible to observe the evolution in the physical properties as function of preparation conditions in the coatings, in agreements of Li and co-workers [56].

In Fig. 21a, b, c, and d, the scanning electron microscopies at ×1000 magnification of the scratch traces for the nc-TiSiCN nanocomposite coatings deposited at different applied powers on the Si_3N_4 target are presented. To observe the critical load effect and cohesive (L_{C1}) and adhesive (L_{C2}) failures on the coating surfaces, the SEM

Fig. 21 Scanning electron microscopy on the scratch traces for all TiSiCN coatings deposited as a function of the applied power on the Si_3N_4 target: **a** 400 W, **b** 450 W, **c** 500 W, and **d** 550 W
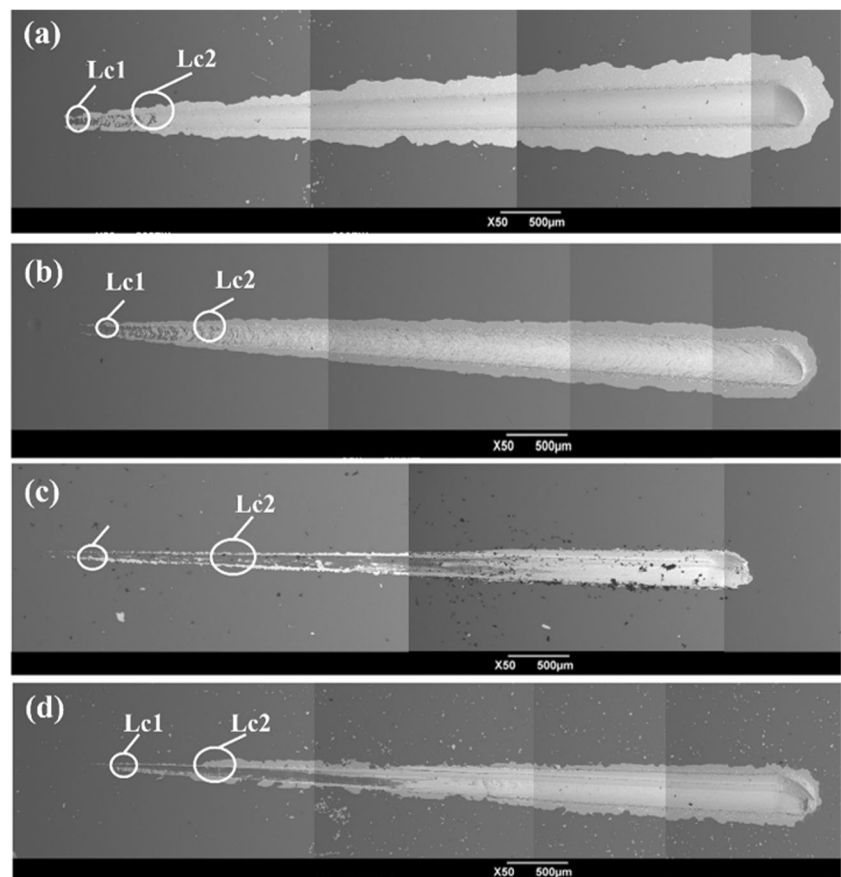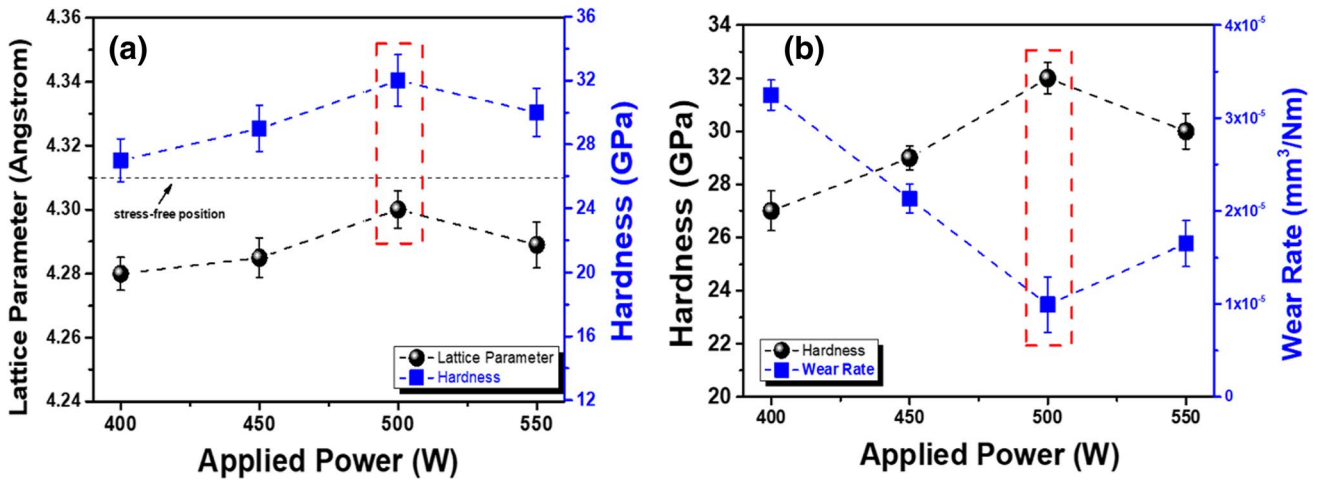
Fig. 22 Merit index for **a** structural and mechanical properties and **b** mechanical and tribological properties

micrographs present that the increase in the critical loads was made when the applied power was increased until a maximum value where a reduction begins. These tribological effects observed by SEM micrographs complement those evidenced in Figs. 17 and 18. Taking into account that the increase in the elastic recovery and the increase in the elastic deformation resistance act as a block to crack propagation, a higher load must be applied to generate cracks and detachment of the coating (adhesive failure) of the substrate/coating system (HSS/TiSiCN).

3.10 Merit index

In order the correlate the obtained properties of the coatings as a function of the applied power. Figure 22a and b show a direct correlation between two different properties as a function of the applied power, where it was possible to show at which power the best set of properties was obtained. Figure 22a shows the correlation between the lattice parameter and hardness, as well as the value of the theoretical lattice parameter (dotted line), where the material is stress-free. From these results, it was possible to show that the coating deposited with 500 W presented a lattice parameter closer to the stress-free position and with the higher hardness obtained (32 GPa); this behavior is attributed to the fact that this structure presented a lower amount of residual stresses during the deposition process, which generated a coating with a more orderly and dense growth than the others, influencing its surface properties such as roughness and grain size. And where these surface properties influenced the resulting mechanical properties of the coating, since having a smaller grain size, a higher grain edge density was obtained, which act as impediments to the passage of dislocations through the coating, which causes an increase in mechanical properties.
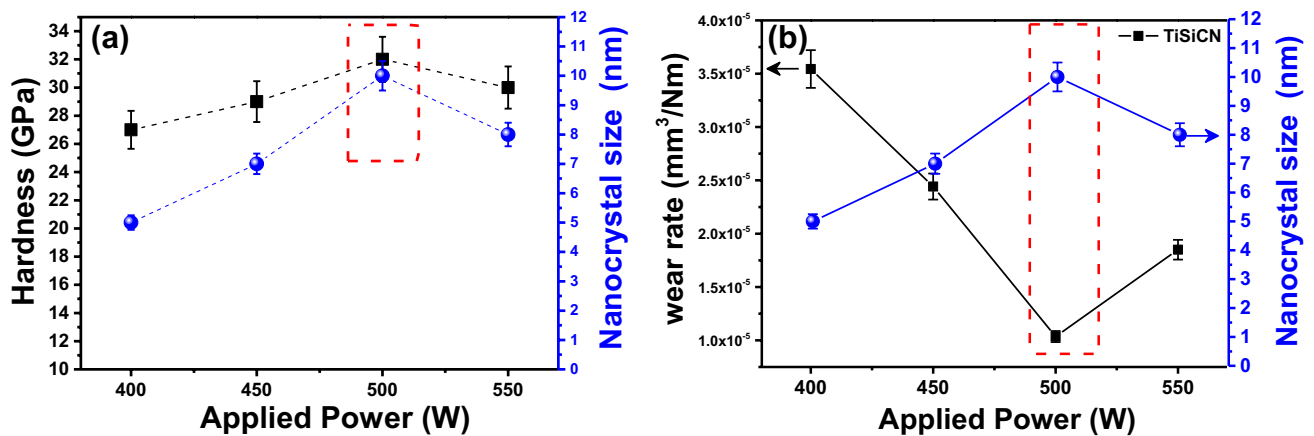

Fig. 23 Merit index for the process variables and the future applications in the industrial field: **a** mechanical properties and nanocrystal size and **b** tribological properties and nanocrystal size as function of applied power on Si_3N_4 target

Figure 22b shows the direct comparison between hardness and wear rate for the coatings obtained as a function of applied power. Through this analysis, it was possible to show that the same trend was maintained, where the coating deposited with 500 W presented a higher hardness and lower wear rate. This mechanical and property behavior is related to the surface characteristics, since having a much more homogeneous surface with higher hardness, as previously presented, generates lower amounts of wear particles, which directly influence the surface wear of the coatings.

Figure 23 shows the variation of hardness, wear rate, and size of the nanocrystals as a function of process variables such as applied power onto Si_3N_4 target (Fig. 23a and b). In that sense when the size of the discrete phase or the crystals size is very low between 5 and 8 nm, the continuous phase (amorphous) tends to be larger; therefore, the mechanical properties, e.g. hardness, tend to decrease when the material is subjected to applied load. In addition, when the crystal size is very low, the plastic deformation or cracks progress easily due to the reduced crystal size, since the nanocrystals act as zones of high symmetry dissipating the crack energy and increasing the mechanical properties, which will be reflected in a better performance of mechanical devices coated with the Ti-Si-C-N nanocomposite.

3.11 Analysis of wear test results

ASSAB 17 steel burins, both uncoated and coated with TiSiCN nanocomposite coatings as machining tools, were incorporated to analyze the wear trend during the machining process. Flank wear (VB) was measured by using scanning electron microscopy (SEM). For a fair comparison, all the coatings have been tested under the same conditions and with the same procedure in accordance with ISO3685 [57]. Therefore, the sources of uncertainties considered in estimating the tool life are flank wear measurement, cutting condition variability (spindle speed and feed rate), and time measurement.

In the present experiments, the typical tool wear pattern is shown in Fig. 24; the integrity of the cutting ASSAB 17 steel uncoated and coated with TiSiCN nanocomposite coatings can be observed. Therefore, the major tool wear mechanisms were interactions of abrasive wear, adhesion wear, microbreakout, and chipping when cutting AISI 1020 steel. The notch wear is a key wear type of ASSAB 17 steel burins when machining AISI 1020 steel at high cutting speeds. The tool wear mechanisms of coated ASSAB 17 steel burins were adhesive, abrasive, and peeling and fracturing of coating.
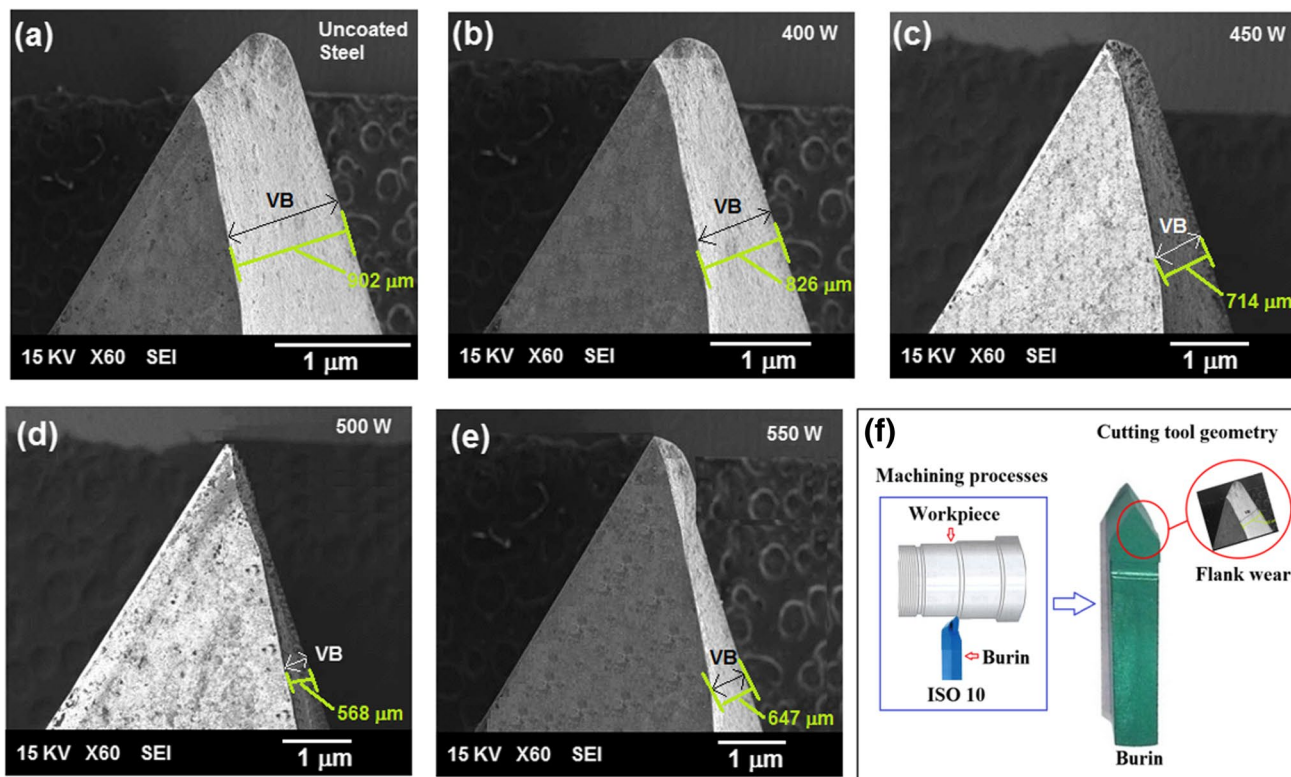

Fig. 24 Worn surface (flank wear) of ASSAB 17 steel burins coated with TiSiCN nanocomposite coatings as function of applied power on Si_3N_4 target: **a** uncoated ASSAB 17 steel burins, **b** steel burins coated with 400 W, **c** steel burins coated with 450 W, **d** steel burins coated with 500 W, **e** steel burins coated with 550 W, and **f** geometric configuration of the workpiece and the cutting tool showing the flank wear

The flank wear of coated ASSAB 17 steel burins was severe during the experiments for ASSAB 17 steel uncoated and coated with TiSiCN nanocomposite coatings; however, the severity of the wear was reduced when the applied power went from 400 to 500 W. Rapid increase in notching at the tool nose leads to tool edge breakout in uncoated ASSAB 17 steel and ASSAB 17 steel coated with lower applied power on Si_3N_4 target (400 W) (Fig. 24a and b); thereby, it is possible to find that uncoated ASSAB 17 steel burin is unsuitable to cut AISI 1020 steel within the experimental cutting speed range. Moreover, the morphology image of wear is evident on the edge of the ASSAB 17 steel (Fig. 24). This wear is generated by the cutting parameter (Table 1), where a reduction in the flank wear (VB) is observed on the ASSAB 17 steel burins coated with TiSiCN nanocomposite coatings. This is in concordance with the mechanical and tribological test when the applied power is increased (Figs. 13, 15, and 19). High hardness and elastic modulus contribute to a reduced friction coefficient between the cutting tool and the

workpiece, conferring superficial hardness that reduces the abrasive wear caused by this interaction. Thus, the grade of ASSAB 17 steel burins coated with higher applied power (500 W) is better than the uncoated ASSAB 17 steel burins at high cutting speed because the TiSiCN coatings with (500 W) provide exceptional resistance to heat and wear, unlike the uncoated ASSAB 17 steel burins and TiSiCN nanocomposite coatings with (400 W); it also demonstrates higher hardness, elastic modulus, and better tribological properties, such as those present in the merit index (Fig. 23); also, the surface damage in uncoated ASSAB 17 steel burin peeling is more severe than that of the ASSAB 17 steel burins with TiSiCN nanocomposite coatings (Fig. 24a, b, c, d, and e). Finally, in Fig. 24f, it is possible to observe the geometric configuration of the workpiece, the cutting tool (burin), and the area of the burin where the flank wear was analyzed via SEM.

Flank wear as a function of cutting length for uncoated and coated ASSAB 17 steel burins with different applied
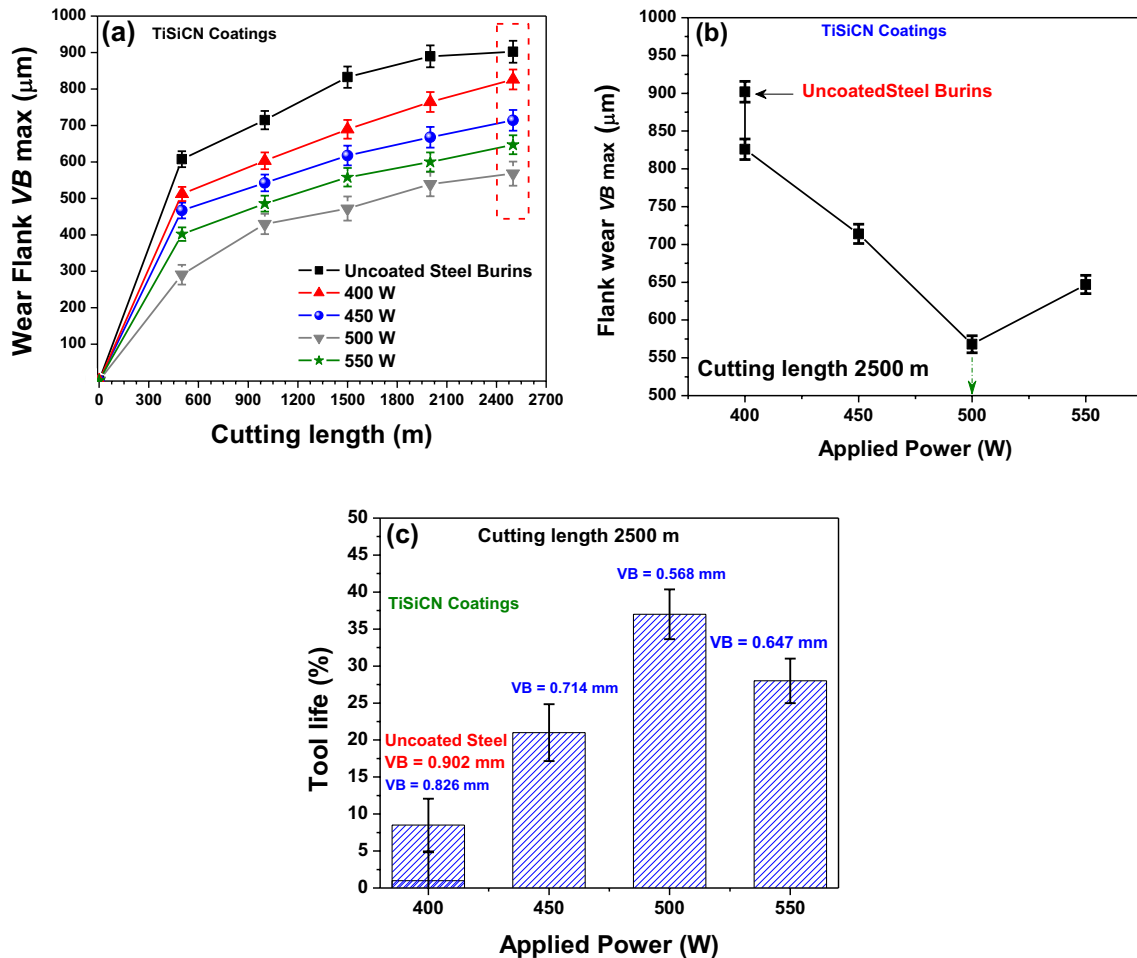

Fig. 25 Wear test results for uncoated ASSAB 17 steel burins and ASSAB 17 steel burins coated with TiSiCN nanocomposite coatings: **a** flank wear (VB) as a function of cutting length, **b** flank wear (VB) as a function of applied power on Si_3N_4 target, and **c** tool life at ASSAB 17 steel burins

power is shown in Fig. 25a. The flank wear (VB) analyses for ASSAB 17 steel were present for 400, 900, 1400, 2000, and 2500 m of cutting length. The steel burins coated with TiSiCN nanocomposite coatings exhibited a lower VB than the uncoated ASSAB 17 steel; the wear increases as function of the applied power reduction (Fig. 25b), as noted in Fig. 25a and b. This behavior corresponds to excessive adhesive wear characteristic for this tribological system when the coating shows delaminating [58]. Additionally, the turning effect on the tool life is presented in Fig. 25c for high cutting speed parameters (Table 1), which corresponds to reduced flank wear from 902 to 568 μm (2500-m cutting length) for ASSAB 17 steel burins uncoated to ASSAB 17 steel burins coated, deposited with 500 W. The good performance (with 37% enhanced tool life) for the ASSAB 17 steel burins coated with high applied power (500 W) present on surface tool material can be attributed to high hardness with relative high elastic modulus (Fig. 13), together with a low friction coefficient (Figs. 15 and 16) and a high critical load (Figs. 19 and 20). This represents exceptional edge wear resistance, high strength, and resistance to deformation and depth of cut notch wear. These properties are adequate enough to endure the thermal and mechanical stresses produced in machining AISI 1020 steel, at this high cutting speed, without suffering the inherent limitations of the PVD coatings (e.g., low adhesion and residual stresses on sharp edges that can induce coating delamination).

4 Conclusions

From r.f magnetron sputtering, a mechanic-tribological [nc-TiSiCN]-[a-SiCN] quaternary nanocomposite coating with crystalline structure of nc-TiSiCN phase accompanied by an amorphous phase of a-SiCN as function of deposition parameters such as applied power target was obtained.

The physical characteristic on the plasma within high vacuum processes as ionic bombardment onto ceramic TiC and Si_3N_4 targets with applied power from 400 to 500 W was able to generate a quaternary material whose reduction in grain size and roughness was 13.4% and 30.7%, respectively.

The generation of a continuous amorphous a-SiCN phase and a discrete nc-TiSiCN phase, with fusiform grain morphology where inhabiting the crystalline phase observed by TEM, was responsible for an increase in the mechanical properties such as hardness from 27 to 32 GPa and elastic modulus from 290 to 301 GPa which was evidenced.

The symmetry breaking in the amorphous crystalline interface of the nanocomposite together with the increase of the nanocrystals generation with the applied power produced an evolution in the tribological properties evidenced by friction coefficient decreasing in relation to uncoated HSS steel; in this sense, the nanocomposite obtained with a power

of 500 W exhibited the best performance showing the lower friction coefficient of 0.31 and lower critical load of 62.4 N, with lower wear rate.

By manipulating the deposition variables with a vacuum control, it was possible to generate nc-TiSiCN nanocomposites with different powers; then, the coating with 500 W showed a reduction in the adhesive and abrasive wear, and this effect was generated by a better sliding counterpart associated to the smaller contact area due to the increase of the mechanical properties, providing an industrial alternative in metal-mechanical components that require a high performance related to the increase in properties such wear resistance.

During the machining process in turning, the wear mechanisms for uncoated and coated ASSAB 17 steel burins were investigated. It was found that adhesive wear and abrasive wear were the principal wear mechanisms, controlling the deterioration and final failure of the ASSAB 17 steel tools. From the qualitative analysis of the coatings compared to the uncoated tools, it was found that the ASSAB 17 steel coated with TiSiCN system with 500 W exhibited the highest wear resistance and the lowest adhesive wear. In addition, this TiSiCN nanocomposite coating exhibited the fewest flank wear values and enhanced tool life of 28% as compared to uncoated ASSAB 17 steel.

Declarations

References

1. Martin PM (2009) Handbook of deposition technologies for films and coatings: science, applications and technology, 3rd edn. https://public.ebookcentral.proquest.com/choice/publicfullrecord.aspx?p=566654
2. Baptista A, Silva FJG, Porteiro J, Míguez JL, Pinto G, Fernandes L (2018) On the physical vapour deposition (PVD): evolution of magnetron sputtering processes for industrial applications. Procedia Manuf 17:746–757. https://doi.org/10.1016/j.promfg.2018.10.125

3. Caicedo JC, Cabrer G, Aperador W, Caicedo HH, Mejia A (2012) Determination of the best behavior among AISI D3 steel, 304 stainless steel and CrN/AlN coatings under erosive-corrosive effect. Vacuum 86:1886–1894

4. Bobzin K (2017) High-performance coatings for cutting tools. CIRP J Manuf Sci Technol 18:1–9. https://doi.org/10.1016/j.cirpj.2016.11.004

5. Caicedo JC, Guerrero A, Aperador W (2017) Physical properties evolution on ternary and quaternary carbonitride coatings. Vacuum. 143:217–224

6. Veprek S, Reiprich S (1995) A concept for the design of novel superhard coatings. Thin Solid Films 268:64–71. https://doi.org/10.1016/0040-6090(95)06695-0

7. Patscheider J (2003) Nanocomposite hard coatings for wear protection. MRS Bull 28:180–183. https://doi.org/10.1557/mrs2003.59

8. Veprek S (1999) The search for novel, superhard materials. J Vac Sci Technol 17:2401–2420. https://doi.org/10.1116/1.581977

9. Voevodin AA, Zabinski JS (2005) Nanocomposite and nanostructured tribological materials for space applications. Compos Sci Technol 65:741–748. https://doi.org/10.1016/j.compscitech.2004.10.008

10. Rafaja D, Poklad A, Klemm V, Schreiber G, Heger D, Šíma M, Dopita M (2006) Some consequences of the partial crystallographic coherence between nanocrystalline domains in Ti–Al–N and Ti–Al–Si–N coatings. Thin Solid Films 514:240–249. https://doi.org/10.1016/j.tsf.2006.02.092

11. Oláh N, Fogarassy Z, Sulyok A, Szívós J, Csanádi T, Balázsi K (2016) Ceramic TiC/a:C protective nanocomposite coatings: structure and composition versus mechanical properties and tribology. Ceram Int 42:12215–12220. https://doi.org/10.1016/j.ceramint.2016.04.164

12. Marchin N, Ashrafizadeh F (2021) Effect of carbon addition on tribological performance of TiSiN coatings produced by cathodic arc physical vapour deposition. Surf Coat Technol 407:126781. https://doi.org/10.1016/j.surfcoat.2020.126781

13. Johnson LJS, Rogström L, Johansson MP, Odén M, Hultman L (2010) Microstructure evolution and age hardening in (Ti,Si)(C,N) thin films deposited by cathodic arc evaporation. Thin Solid Films 519:1397–1403. https://doi.org/10.1016/j.tsf.2010.08.150

14. Lin J, Wei R, Bitsis DC, Lee PM (2016) Development and evaluation of low friction TiSiCN nanocomposite coatings for piston ring applications. Surf Coat Technol 298:121–131. https://doi.org/10.1016/j.surfcoat.2016.04.061

15. Thangavel E, Lee S, Nam K-S, Kim J-K, Kim D-G (2013) Synthesis and characterization of Ti–Si–C–N nanocomposite coatings prepared by a filtered vacuum arc method. Appl Surf Sci 265:60–65. https://doi.org/10.1016/j.apsusc.2012.10.107

16. Greczynski G, Hultman L (2020) X-ray photoelectron spectroscopy: towards reliable binding energy referencing. Prog Mater Sci 107:100591

17. ASTM (2015) E1523-15. Standard guide to charge control and charge referencing techniques in X-ray photoelectron spectroscopy. West Conshohocken (PA), ASTM International www.astm.org

18. ISO 19318:2004. Surface chemical analysis – reporting of methods used for charge control and charge correction

19. ISO 15472:2010. Surface chemical analysis – X-ray photoelectron spectrometers – Calibration of energy scales (ISO, Geneva, 2010)

20. Seah MP (2001) Summary of ISO/TC 201 Standard: VII ISO 15472: 2001—surface chemical analysis—X-ray photoelectron spectrometers—calibration of energy scales. Surf Interface Anal 31:721–723

21. ISO 16243:2011s Surface chemical analysis — recording and reporting data in X-ray photoelectron spectroscopy (XPS)

22. ISO 18516:2019 Surface chemical analysis Determination of lateral resolution and sharpness in beam-based methods with a range from nanometres to micrometres and its implementation for imaging laboratory X-ray photoelectron spectrometers (XPS)

23. Greczynski G, Hultman L (2021) The same chemical state of carbon gives rise to two peaks in X-ray photoelectron spectroscopy. Sci Rep 11:11195

24. Evans S (1973) Work function measurements by X-Pe spectroscopy, and their relevance to the calibration of X-Pe spectra. Chem Phys Lett 23:134–138

25. ASTM International (2017) Standard Test method for wear testing with a pin-on-disk apparatus G99-17. Annu B ASTM Stand 05:1–6. https://doi.org/10.1520/G0099-17.Copyright

26. Method ST (2003) Scratch hardness of materials using a diamond stylus. Current. 14:1–7. https://doi.org/10.1520/G0171-03R17.2

27. Nledengvist P, Hogmark S (1997) Experiences from scratch testing of tribological PVD coatings. Tribol Int 30:507–516

28. Lin Y-C, Hsu S-Y, Song R-W, Lo W-L, Lai Y-T, Tsai S-Y, Duh J-G (2020) Improving the hardness of high entropy nitride (Cr0.35Al0.25Nb0.12Si0.08V0.20) N coatings via tuning substrate temperature and bias for anti-wear applications. Surf Coat Technol 403:126417. https://doi.org/10.1016/j.surfcoat.2020.126417

29. Anandh Jesuraj S, Kuppusami P, Ajith Kumar S, Panda P, Udaiyappan S (2019) Investigation on the effect of deposition temperature on structural and nanomechanical properties of electron beam evaporated lanthanum zirconate coatings. Mater Chem Phys 236:121789. https://doi.org/10.1016/j.matchemphys.2019.121789

30. Arunkumar P, Ramaseshan R, Dash S, Basu J, Ravindran TR, Balakumar S, Babu KS (2014) Texturing of pure and doped CeO2 thin films by EBPVD through target engineering. RSC Adv 4:33338–33346. https://doi.org/10.1039/c4ra04353g

31. Ortiz CH, Aperador W, Caicedo JC (2022) Physical properties evolution of β-tricalcium phosphate/hydroxyapatite heterostructures in relation to the bilayer number. Thin Solid Films 752:139256. https://doi.org/10.1016/j.tsf.2022.139256

32. Ortiz CH, Aperador W, Caicedo JC (2022) Electrochemical response of (β-TCP and HA) individual coatings and [β-TCP/HA] multilayers coatings exposed to biocompatible environments. Surf Coat Technol 435:128266. https://doi.org/10.1016/j.surfcoat.2022.128266

33. Ortiz CO, Colorado HD, Aperador W, Jurado A (2019) Influence of the number of bilayers on the mechanical and tribological properties in [TiN/TiCrN]n multilayer coatings deposited by magnetron sputtering. Tribol Ind 41:330–343. https://doi.org/10.24874/ti.2019.41.03.03

34. Greczynski G, Hultman L (2017) C1s peak of adventitious carbon aligns to the vacuum level: dire consequences for material's bonding assignment by photoelectron spectroscopy. ChemPhysChem. 18:1507–1512

35. Greczynski G, Hultman L (2020) Compromising science by ignorant instrument calibration—need to revisit half a century of published XPS data. Angew Chem 132:5034–5038

36. Anju VG, Austeria MP, Sampath S (2017) Work function tunable titanium carbonitride nanostructures for high-efficiency, rechargeable Li–iodine batteries. Adv Mater Interfaces 4:1700151

37. Greczynski G, Hultman L (2018) Reliable determination of chemical state in x-ray photoelectron spectroscopy based on sample-work-function referencing to adventitious carbon: resolving the myth of apparent constant binding energy of the C 1s peak. Appl Surf Sci 451:99–103

38. Li J, Wang Y, Yao Y, Wang Y, Wang L (2017) Structure and tribological properties of TiSiCN coating on Ti6Al4V by arc ion plating. Thin Solid Films 644:115–119. https://doi.org/10.1016/j.tsf.2017.09.053

39. Lin J, Wei R (2018) A comparative study of thick TiSiCN nanocomposite coatings deposited by dcMS and HiPIMS with and without PEMS assistance. Surf Coat Technol 338:84–95. https://doi.org/10.1016/j.surfcoat.2018.01.082

40. Wang Y, Li J, Dang C, Wang Y, Zhu Y (2017) Influence of carbon contents on the structure and tribocorrosion properties of TiSiCN

coatings on Ti6Al4V. Tribol Int 109:285–296. https://doi.org/10.1016/j.triboint.2017.01.002

41. Ma Y, Yang J, Tian X, Gong C, Zheng W, He Y, Li H, Gao Z, Zhang K, Wei L, Chu PK (2020) Enhanced discharge and surface properties of TiSiCN coatings deposited by pulse-enhanced vacuum arc evaporation. Surf Coat Technol 403:126413. https://doi.org/10.1016/j.surfcoat.2020.126413

42. Wang R, Yang C, Hao J, Shi J, Yan F, Zhang N, Jiang B, Shao W (2022) Influence of target current on structure and performance of Cu films deposited by oscillating pulse magnetron sputtering. Coatings 12:394. https://doi.org/10.3390/coatings12030394

43. Matsutani T, Tai Y, Kawasaki T (2020) Nitrogen ion beam thinning of a-SiCN diaphragm for environmental cell prepared by low-energy ion beam enhanced chemical vapor deposition. Vacuum. 182:109770

44. Ma X, Mao Z, Xu D, Ding Y, Xu C (2020) High-rate synthesis of SiCN films using single-source silicon precursor with high-density helicon plasma. Vacuum. 177:109397

45. Hernandez-Rengifo E, Ortiz CH, Hidalgo CH, Ballesteros JA, Caicedo JC (2021) Comparative study of tribological and mechanical properties between single layers of Al_2O_3 and Si_3N_4 deposited on AISI 316 stainless steel. Tribol Ind 43:259–273. https://doi.org/10.24874/ti.956.09.20.01

46. Ortiz CH, Hernandez-Rengifo E, Guerrero A, Aperador W, Caicedo JC (2021) Mechanical and tribological properties evolution of $[Si_3N_4/Al_2O_3]$n multilayer coatings. Tribol Ind 43:23–39. https://doi.org/10.24874/ti.952.08.20.01

47. Endler I, Höhn M, Schmidt J, Scholz S, Herrmann M, Knaut M (2013) Ternary and quarternary TiSiN and TiSiCN nanocomposite coatings obtained by chemical vapor deposition. Surf Coat Technol 215:133–140. https://doi.org/10.1016/j.surfcoat.2012.10.067

48. Zheng Y-j, Yong-xiang Leng X, Xin Z-y X, Fan-qingJiang R, Wei NH (2013) Evaluation of mechanical properties of Ti(Cr)SiC(O)N coated cemented carbide tools. Vacuum. 90:50–58

49. Piedrahita WF, Aperador W, Caicedo JC, Prieto P (2017) Evolution of physical properties in hafnium carbonitride thin films. J Alloys Compd 690:485–496

50. Archard JF (1953) Contact and rubbing of flat surfaces. J Appl Phys 24:981–988. https://doi.org/10.1063/1.1721448

51. Pierson HO (1996) Carbides of group IV. In: Handbook of Refractory Carbides and Nitrides. Elsevier, pp 55–80. https://doi.org/10.1016/B978-081551392-6.50005-2

52. Ortiz Ortiz C, Hernandez-Rengifo E, Cesar Caicedo J (2021) Analysis of the tribological evolution of nitride-based coatings. In: Tribol. [Working Title. IntechOpen. https://doi.org/10.5772/intechopen.100629

53. Fernandes L, Silva FJG, Paiva OC, Baptista A, Pinto G (2018) Minimizing the adhesion effects in food packages forming by the use of advanced coatings. Procedia Manuf 17:886–894. https://doi.org/10.1016/j.promfg.2018.10.141

54. Falsafein M, Ashrafizadeh F, Kheirandish A (2018) Influence of thickness on adhesion of nanostructured multilayer CrN/CrAlN coatings to stainless steel substrate. Surf Interfaces 13:178–185. https://doi.org/10.1016/j.surfin.2018.09.009

55. Sunil J, Godwin J, Selvam CM (2020) Roles of nanomaterials at the rubbing interface of mechanical systems. Mater Today Proc 21:184–188. https://doi.org/10.1016/j.matpr.2019.04.218

56. Li Q, Jiang F, Leng Y, Wei R, Huang N (2013) Microstructure and tribological properties of Ti(Cr)SiCN coating deposited by plasma enhanced magnetron sputtering. Vacuum. 89:168–173

57. Panda A (2012) Analysis of cutting tools durability compared with standard ISO 3685. Int J Adv Comput Theory Eng 4(4):621–624

58. Coelho RT, Ng E-G, Elbestawi MA (2007) Tool wear when turning hardened AISI 4340 with coated PCBN tools using finishing cutting conditions. Int J Mach Tools Manuf 47(2):263–272